NTNU

Norwegian University of
Science and Technology

Exploring Electronic Confinement in Si:P δ-layers

Thomas Nyborg

Master of Science
Submission date: June 2018
Supervisor: Justin Wells, IFY

Norwegian University of Science and Technology
Department of Physics

Abstract

In this thesis, the electronic states of a quantum well system in silicon is investigated. The confinement is induced by a thin dopant profile called a δ-layer, creating an effective two-dimensional metallic region inside a semiconducting bulk environment. The understanding of these systems is of great importance for silicon-based quantum computing applications, which rely on exact knowledge of the dynamics of the quantum well states. The presented results serve to complement existing work in this field, which has mainly been focused towards the extreme case of a single atomic layer dopant profile. Five silicon-phosphorus δ-layer samples with different dopant profile thickness were fabricated by gas dosing and epitaxial growth. The electronic band structure was investigated using angle-resolved photoemission spectroscopy (ARPES) and synchrotron radiation. The energy separations of the three lowest electronic energy bands, known as the 1Γ, 2Γ and 1Δ, were tracked as the δ-layer thickness was changed. Most notably, novel measurements of the 1Δ state in a monolayer is presented, allowing sought-after comparison to existing work. The results suggest taking an alternate view of the band structure in these devices, specifically by reinterpreting the identification of the Γ states in observations. This new picture speaks in favor of adopting a larger material dielectric constant than previously assumed for these structures, which can reduce current inconsistencies between experimental observations and calculations.

Sammendrag

I denne masteroppgaven undersøkes elektrontilstandene i et kvantebrønn-system i silisium. Ved å introdusere et tynt, sterkt dopet lag i en silisiumkrystall, kalt et δ-lag, skapes en tilnærmet to-dimensjonal metallisk profil inne i et halvledermateriale. Dette medfører interessante elektroniske egenskaper som kan utnyttes innenfor utviklingen av silisium-baserte kvantedatamaskiner. Forståelse av hvordan disse systemene oppfører seg er svært viktig for mulige anvendelser, som krever presis manipulering av kvantiserte energitilstander som oppstår i laget. Resultatene som presenteres vil være et tillegg til eksisterende forskning på disse strukturene, som hovedsaklig omhandler spesialtilfellet der δ-laget er kun ett atomlag tykt (såkalt monolag). Det ble laget fem δ-lag med forskjellig tykkelse som ble undersøkt med "angle-resolved photoemission spectroscopy" (ARPES). Energidifferansen mellom de tre laveste energitilstandene i laget, kjent som 1Γ, 2Γ og 1Δ, ble sett i sammenheng med endringene i tykkelse. 1Δ tilstandene ble observert for første gang i et monolag, som gjorde det mulig å sammenligne med eksisterende data. Resultatene peker mot en endring av forståelsen av båndstrukturen, spesielt ved å revidere hvordan Γ tilstandene har blitt identifisert i tidligere eksperimentelle data. Dette kan ses i sammenheng med en endring i verdien av den dielektriske konstanten i forhold til hva som tidligere har blitt antatt. Dette kan bidra til å minske uoverenstemmelser mellom teoretiske beregninger og praktiske observasjoner, som har satt spørsmålstegn ved den etablerte forståelsen av slike strukturer.

Preface

In writing this thesis I have been so lucky to be a part of new, exciting research related to the relevant and expanding field of quantum computing. I am honored to have been given this opportunity. Several people deserve my thanks and appreciation for supporting me in this work. First of all, I would like to thank my supervisor Justin Wells for the freedom and support you have given me throughout my time as a Master's student in the group. I admire your faith in your students and their abilities to accomplish something great, your respect for everyone's opinion regardless of their title or prefix, and your ability to provide interesting anecdotes on just about any subject. The informal, social, yet highly professional environment you have established in the group has been truly motivating. I would also like to extend my sincere gratitude to Ph.D. student Ann Julie Utne Holt from the surface physics group at Aarhus University for the invaluable cooperation, both before, during and after beamtime. This thesis would not have come together without your help. Last but not least, I wish to thank Alex Schenk, postdoc in our group, for educating me in the wonders of photoemission and the mysteries of UHV systems. Thank you for helping me out, in both real and reciprocal space, and for putting up with all my questions at any hour of the day (after 10 am).

-

The measurements presented in this thesis are a result of cooperation between our group at NTNU and the surface physics group at Aarhus University, Denmark. I want to use this opportunity to acknowledge this contribution to providing the experimental basis for this thesis.

Thank you.

Trondheim, June 2018

Thomas Nyborg

Contents

List of Figures

List of Abbreviations

2DEG two-dimensional electron gas

ARPES angle-resolved photoemission spectroscopy

ASTRID Aarhus storage ring in Denmark

BZ Brillouin zone

CBM conduction band minima

DFT density functional theory

EDC energy distribution curve

EMT effective mass theory

MDC momentum distribution curve

ML monolayer

SW square well

TB tight-binding

UHV ultra-high vacuum

VBM valence band maxima

XPS X-ray photoemission spectroscopy

Chapter 1

Introduction

1.1 Motivation for this thesis

The study of quantum effects in low-dimensional semiconductor systems constitute a key part of the progress of solid state physics in the past decades. Thin films, multilayered structures, and quantum dots are increasingly present in modern electronic devices, where size-effects such as quantum well confinement are central to device operation [31]. In recent years, atomic-scale precision in semiconductor doping manipulation has been demonstrated; an important advancement with respect to the practical realization of quantum computing systems. Phosphorus dopant structures in silicon were the basis for one of the first proposals for a solid-state quantum computer architecture [12, 19], and have since been extensively studied in the attempt of gaining insight into the electronic properties of such devices. Recently developed patterning techniques offers the possibility of assembling elaborate structures which are relevant to quantum computing applications, such as the single-atom transistor (see Figure 1.1). A thorough understanding of the electronic state configuration of such structures is crucial to predicting and controlling device operation. Thin, heavily phosphorus-doped sheets inside a bulk silicon environment, called Si:P δ-layers, represent both an

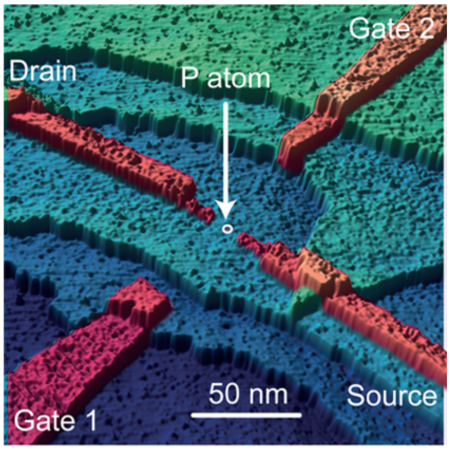

Figure 1.1: Single-atom transistor. Patterned, heavily phosphorus-doped silicon leads (red features) are used to address a single phosphorus atom (center) inside bulk silicon. Reprinted from Ref. [34].

important platform for base research on these systems as well as being a promising candidate for hosting quantum computer architectures [28–30]. The atomically sharp doping profile, called a monolayer, has become the most prominent objective of silicon δ-layer research, as this represents the most relevant configuration for application purposes. However, discrepancies between certain theoretical predictions and experimental observations have led to concerns regarding the reliability of the current theoretical description of these systems. Additional studies of thicker dopant layers may lead to an increased understanding of the situation by allowing trends of the energy states to be seen as the character of the states are modified. The work presented in this thesis aims to contribute to this purpose, specifically by tracking the behavior of the electronic states of a δ-layer as the thickness is altered from bulk-like to a truly two-dimensional case.

1.2 Layout

A theoretical framework for describing electronic states in a solid is presented in Chapter 2. Some general properties will first be treated before turning to the specific case of silicon δ-layers. Relevant existing work will be presented to identify the status quo of the research directed towards these structures, including some important calculations and experimental observations made to this date. This will set the stage for the work conducted in relation to this thesis. Chapter 3 is devoted to presenting the techniques involved in the characterization and preparation of the δ-layer structures. The practical aspect of the experimental work carried out is documented in Chapter 4, where the instrumentation and the specifics of the sample preparation process is presented. The width-dependence of the δ-layer electronic states is not much studied, and a thorough theoretical model for this specific case is not found in the existing literature. Therefore, a simple numerical model is presented in Chapter 5 to supplement existing work when discussing the results. In Chapter 6, the results will be presented and discussed in light of the previous chapters. The thesis is concluded in Chapter 7 where the main findings from the discussion is summarized and further work is suggested. Additional information supplementing the main text is given in the Appendix.

Chapter 2

Theoretical background

The purpose of this chapter is to give a primer of the subject, including key theoretical aspects and previous work defining the basis of the experiment described by this text. I will begin by presenting some fundamental properties of crystals, before advancing to the theoretical description of electron states in crystal structures. This will be used to give a brief treatment of key semiconductor properties. These parts are largely based on Ref. [15, 16], and the reader is directed to these resources for additional details. Towards the end of the chapter I will focus on the specific case of silicon δ-layer structures.

2.1 Crystal structure

2.1.1 The crystal lattice

A crystal is a periodic structure which in principle can be described by a infinite set of points on a lattice, defined by the linear combination of a particular set of primitive lattice vectors. Such a lattice is called a *Bravais lattice*. By translating from one point in the lattice to another through a lattice-specific displacement vector $\mathbf{r}$ (i.e. any linear combination of the primitive lattice vectors), the lattice should look the same as the initial location. The region closer to one lattice point than any other is called the *Wigner-Seitz cell*. This concept is illustrated in Figure 2.1. In addition to a Bravais lattice, real crystal are described by a *basis*, which indicates a particular configuration of atoms associated with a single lattice point.

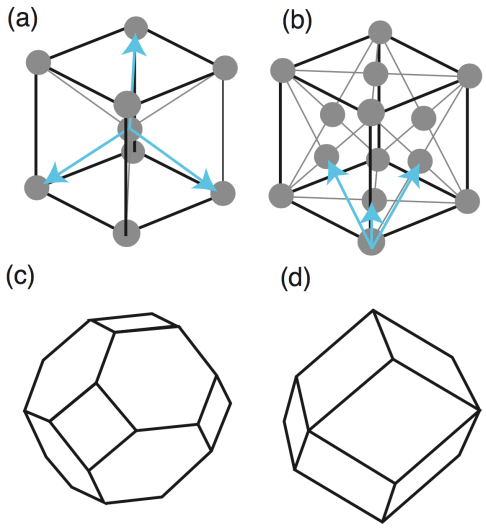

Figure 2.1: Crystal Bravais lattice and Wigner-Seitz cell. (a) Body-centered cubic (bcc) and (b) face-centered cubic (fcc) Bravais lattices. The blue arrows represent the primitive lattice vectors spanning the lattice. (c) The bcc and (d) fcc Wigner-Seitz cells, indicating the spacial region which is closer to the lattice point in the center of the figure than to other lattice points in the Bravais lattice. Reprinted from Ref. [16].

2.1.2 The reciprocal lattice

The reciprocal lattice is the set of wave vectors $\mathbf{G}$ that yield plane waves with the periodicity of the Bravais lattice [16]. This imposes the relation

$$e^{i\mathbf{G}\cdot\mathbf{R}} = 1, \tag{2.1}$$

where $\mathbf{R}$ is the previously defined real space lattice point vector and $\mathbf{G}$ is a reciprocal lattice vector. Just as the vectors $\mathbf{R}$ form a real space Bravais lattice, the vectors $\mathbf{G}$ form a reciprocal Bravais lattice. The reciprocal space equivalent to the Wigner-Seitz cell is the *first Brillouin zone* (1BZ). It is also common to refer to higher order Brillouin zones to indicate the second closest region to a point etc. The reciprocal lattice represents a very handy tool for dealing with the complexity of crystal structures by exploiting the periodicity of the lattice, as we shall see in the next section.

It is convenient to adapt a definition of describing planes and directions in crystal structures. This is done by so-called *Miller indices*, which correspond to planes perpendicular to reciprocal lattice vectors. They are identified by three numbers *hkl* which refer to the components of the reciprocal lattice vector $\mathbf{G}$. A plane is described by the notation (hkl), while {hkl} indicate a family of equivalent

planes. A similar convention applies for real space directions, only now with the indices *l,m,n* referring to the components of **R**. Here, square brackets are used for indicating a real space direction; [lmn].

2.2 Electronic states in solids

In order to describe the electronic states in doped silicon which the work of this text concerns itself with, it is necessary to present a theoretical framework that accurately depicts the physical situation inside a semiconducting material. For this I will use the free- and nearly free electron model. The former is only a good approximation for metals, and will mainly be used as a stepping-stone for the latter. It must be noted that these models are mere approximations, and only serve to illustrate the concept of the electronic states. Still, this will suffice for the purpose of this thesis. A more powerful model when it comes to covalently bond solids like silicon is the tight-binding approach, which will not be treated in this text.

The models I present are based on a quantum mechanical approach to describing electrons in solids. By taking this view, we wish to describe the motion of the electrons by so-called wavefunctions, which contain information about the quantum mechanical eigenstates of the electrons in our system. However, finding the eigenstates of such a complex environment as a solid is an immense task, and we must make a few approximations to make headway. To begin, we separate the atoms in the solid into two parts - the ions and the electrons. The ions consist of the atom nucleus and the tightly bound core electrons. In our treatment, the core electrons can be considered inert due to its strong bonds to the nucleus, and are mostly responsible for shielding the positive nuclear charges [23]. The valence electrons are on the other hand loosely bound to the nucleus, and play a key role for the electronic properties of solids. Based on this basis, the models make two key assumptions:
1) The motion of the ions can be ignored.
2) The correlated motion of the valence electrons can be ignored, and instead described by an effective potential.
Both can be shown to be reasonable approximations for our case [15]. With this in mind, the task at hand is to solve the stationary Schrödinger equation for the eigenstates of single electron, which now reads

$$\Big(-\frac{\hbar^2}{2m_e}\nabla^2 + U(\mathbf{r})\Big)\Psi(\mathbf{r}) = E\Psi(\mathbf{r}). \tag{2.2}$$

Here, $\hbar$ is the reduced Planck constant, m_e is the electron mass, ∇ is the vector differential operator, U is the effective potential, $\mathbf{r}$ is a real space position vector,

Ψ is the electron wavefunction and E is the energy of an electron state.

2.2.1 The free electron model

In the free electron model, we assume that the potential experienced by a single electron is zero, and the problem becomes equivalent to the famous particle in a box problem. The solutions for Ψ are plane waves of the form $Ae^{i\mathbf{kr}}$, where A is a normalization factor, i is the imaginary unit and $\mathbf{k}$ is the electron wave vector[1]. The energy eigenvalues are

$$E(\mathbf{k}) = \frac{\hbar^2 k^2}{2m_e}. \tag{2.3}$$

This is similar to truly free electrons. Applying periodic boundary conditions[2] of the lattice lead to restrictions on the allowed values of the electron momentum described by $\mathbf{k}$. This in turn gives quantized energy levels, such that we get a quasi-continuum of allowed states for the electron momentum and energy. The dispersion relation $E(\mathbf{k})$ is known as the *electronic band structure* of the solid.

Electrons are fermions and thus obey the Paulí exclusion principle, with the implication that no two electrons can occupy the same quantum mechanical state. Energy states are spin-degenerate, such that they can accommodate two electrons with opposite spin; one in the *spin-up*-state and the other in *spin-down*. This means that a system of N electrons in the free electron will model occupy the $N/2$ lowest energy states, assuming zero temperature [15]. The energy of the highest occupied state is the *Fermi energy*, and the number of available energy states per energy interval is called the *density of states*. At finite temperature, electrons are excited out of their ground state. Electrons obey Fermi-Dirac statistics, and the probability of a state being occupied at a given energy E and temperature T is given by the distribution function[3]

$$f(E,T) = \frac{1}{e^{(E-\mu)/k_B T} + 1}, \tag{2.4}$$

where μ is the so-called *chemical potential* and k_B is the Boltzmann constant. At $T = 0$, the chemical potential is equal to the Fermi energy [15]. The Fermi energy has a rigid definition, and due to the statistical implications of the Fermi-Dirac distribution it is convenient to introduce the *Fermi level*, which can be

[1] It is common to use the wave vector in reciprocal space, $\mathbf{k}$, to describe the momentum of the electron, $\mathbf{p}$, which I will continue to do from here on. The quantities are related by the Planck constant: $\mathbf{p} = \hbar\mathbf{k}$.

[2] Periodic boundary conditions, such as the Born-von-Kármán, are useful for describing bulk states and properties related to traveling wave solutions. For treating situations close to a surface, or quantum wells, other boundary conditions are required, as we shall see later on.

[3] This function will later be reffered to as simply the *Fermi function*.

interpreted as the hypothetical energy of a state having a 50% chance of being occupied. For semiconductors, we merely treat the Fermi level as a synonym for the chemical potential [3]. From this an important result arise: The product of the density of states and the Fermi-Dirac distribution gives us the density of occupied electron states (DOS) at a given energy for a finite temperature, effectively giving a probabilistic description of the occupancy of electron states in a solid. This is illustrated by Figure 2.2.

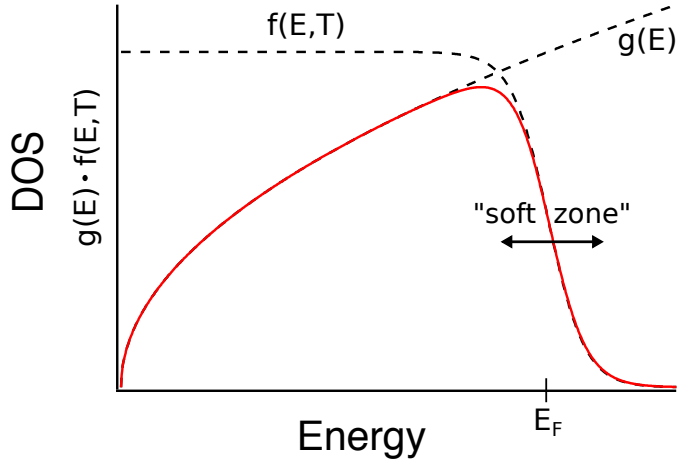

Figure 2.2: Density of occupied electron states (DOS) for finite temperature. The density of states in the free electron model $g(E)$, is modulated by a temperature dependent Fermi-Dirac distribution $f(E,T)$ to produce the density of occupied states (red curve). The broadened region around the Fermi level E_F is referred to as the "soft zone", having a width of ≈ 100 meV at room temperature.

This is all well and good, however; we know that the free electron model can not accurately represent the full picture of electrons in real solid, as it contains no assumptions of a lattice potential. This must surely be present due to the ions sitting on the lattice sites. So, how can we describe the situation of the electron states more precisely? For this feat, we turn to a slightly modified approach, the *nearly-free electron model*.

2.2.2 The nearly-free electron model

The key to effectively describing the electron states is to exploit the symmetry of the crystal structure. In the nearly-free electron model we seek to describe the motion of the electrons in a finite, periodic potential. A solution to the Schrödinger equation that fulfills our demands is of the form

$$\Psi_{\mathbf{k}}(\mathbf{r}) = e^{i\mathbf{k}\cdot\mathbf{r}} u_{\mathbf{k}}(\mathbf{r}). \tag{2.5}$$

This solution is called a *Bloch wave*, where the modifying term $u_{\mathbf{k}}(\mathbf{r})$ contain information about the potential, exhibiting the same periodicity as the real space Bravais lattice. The subscript $\mathbf{k}$ indicates that there shape of the solutions are dependent on the electron momentum. It can be shown that the relation

$$\Psi_{\mathbf{k}+\mathbf{G}}(\mathbf{r}) = \Psi_{\mathbf{k}}(\mathbf{r}) \tag{2.6}$$

holds, meaning that a Bloch wave is only unique up to a shift of a reciprocal lattice vector $\mathbf{G}$. Inserting this back into the Schrödinger equation, one arrives at the relation

$$E(\mathbf{k}+\mathbf{G}) = E(\mathbf{k}) \ , \tag{2.7}$$

which means that the energy also is lattice periodic. Thus, we only need to concern ourselves with the treatment of the system in the first Brillouin zone, as this will include all unique eigenstates of the electrons.

Let us now look at some of the results these models produce, illustrated in Figure 2.3. We have seen that the free electron model yield a parabolic dispersion for the energy with respect to the momentum vector (panel a). By introducing a small, finite potential and imposing the symmetry of the lattice, the energy dispersion is reproduced for shifts of a reciprocal lattice vector (panel b). As the main result of the nearly-free electron model, an increased potential leads to the formation of gaps at the Brillouin zone boundaries, producing regions where there exist no electron energy states (panel c). These regions are known as *band gaps*, while the regions that have available states are the allowed *energy bands*. This result is of great significance for understanding semiconductor properties, which I will return to in Section 2.3.1.

Near the edges of an allowed energy band the energy-momentum relation can be described in a simple way by introducing the *effective mass* of an electron in the solid. By this quantity it is possible to describe the behavior of an electron in the crystal as a free electron with an apparent effective mass m^*. In this way, the effective mass carries information about the internal effects of the lattice potential, representing the response of the electron-crystal system to the outside world [32]. If we now assume that the energy-momentum relation can be described as given by Eq. 2.3, the curvature of the band becomes

$$\frac{d^2E(\mathbf{k})}{dk^2} = \frac{d^2}{dk^2}\left(\frac{\hbar k^2}{2m^*}\right) = \frac{\hbar}{m^*}. \tag{2.8}$$

Thus, we see that the inverse curvature of the band near the band edge becomes a measure of the effective mass of the band.

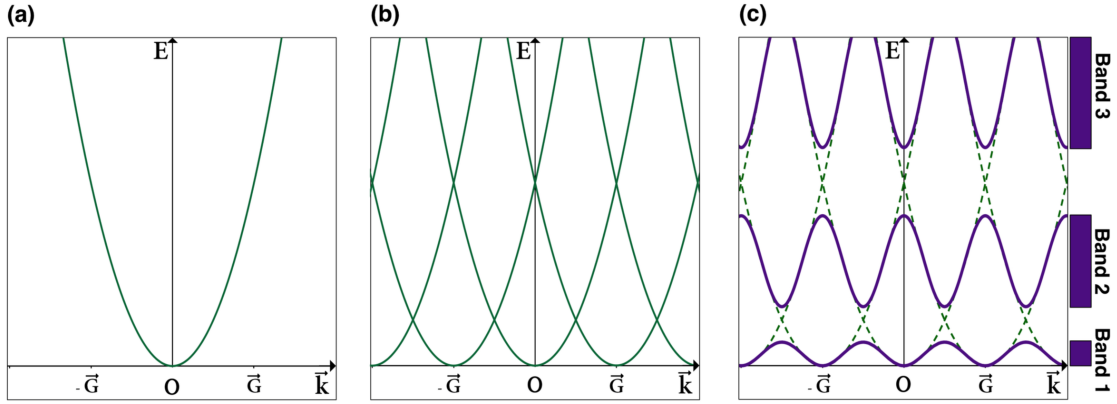

Figure 2.3: Solutions for the electron band structure $E(\mathbf{k})$ for the free- and nearly-free electron model. (a) Free electron case. The energy disperses parabolically as a function of the momentum **k**. (b) When introducing a weak potential and imposing the symmetry of the real lattice, the free electron-like parabolas are reproduced periodically by the displacement of a reciprocal lattice vector **G**. (c) By increasing the effective potential, gaps are formed at the Brillouin zone boundaries, representing energy regions where there are no available energy states. Reprinted from Ref. [17].

2.2.3 Bulk- and surface states

The models used for describing the electronic states are idealistic in the sense that they assume a infinite solid wherein the electrons reside. In real solids, we have to account for the existence of a surface, which effects the Bloch wave solutions for the electrons in the solid. The existence of a surface has two main implications on the electronic states. First of all, the wavefunction of a electron inside the crystal has to vanish outside of the solid. Such solutions can be achieved by matching the wavefunction to an exponential decay at the surface [7, 15]. These states are called *bulk states*. Second, the surface makes a new type of solution possible, originating from a complex part of the **k**-vector. This solution has an oscillating part which grows exponentially towards the surface, and decreases exponentially outside the solid. These states are highly localized to the surface, and are thus named *surface states* [16]. The bulk and surface states are sketched in Figure 2.4.

While the surface breaks the periodicity of the lattice in the direction perpendicular to the surface, it is still present in its parallel direction. As a result, surface states lose their dependence on the perpendicular component of the wave vector while retaining the dependence in the parallel direction, making them effectively two-dimensional. This is an example of two dimensional quantum confinement. In the next section I will look at how quantum confinement can occur in a potential step inside a solid, and how this affect the electronic states.

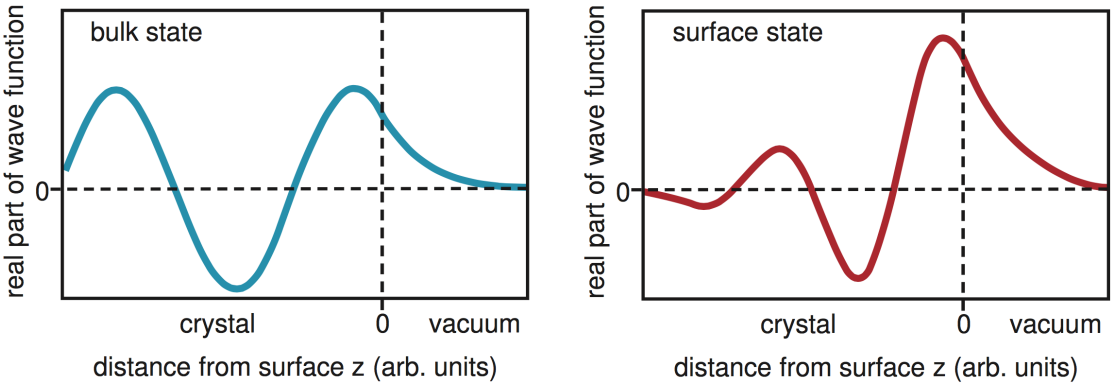

Figure 2.4: Bulk and surface electronic states. The distance z is directed along the axis perpendicular to the surface. (a) The shape of a bulk state wavefunction. For a bulk state, the Bloch wave needs to match a exponential decay at the surface. (b) A surface state wavefunction. When introducing a surface, new states are made possible. Such states are highly localized to the surface, and consist of a oscillating part that is modulated by exponential decays both into the solid and out into vacuum. Reprinted from Ref. [16].

2.2.4 Quantum well states

The concept of a quantum well is central in this thesis, as it is the phenomenon responsible for the electronic states we wish to investigate. We now consider a ideal square potential well in the z-direction in the bulk of a solid. Inside the potential well the electron wavefunction can be split into a parallel and a perpendicular component relative to the potential step [15]. For the parallel wavefunction, the solutions are the same (up to a constant potential offset) as for a nearly-free electron bulk state. The solutions for the wavefunction perpendicular to the potential well must satisfy the boundary conditions of the well. This is a well known problem in quantum mechanics, and leads to discrete quantized energy levels in the z-direction which are significantly separated in energy [15]. This means that there will be confined energy states in the well, trapping electrons in the perpendicular direction. The confinement, and thus the energy separation, depend mainly on two parameters: the width of the well and the strength of the potential [7]. This will be used as a basis to model the width-dependence of confined states in a δ-layer system, which is presented in Chapter 5.

2.3 Quantum confinement in silicon δ-layers

So far we have looked at various forms of electronic states in a crystalline solid, which were derived from a quantum mechanical point of view. Before I continue with the specific case of quantum wells in silicon, I will now briefly look at how this can be extended to describe the theoretical fundamentals of semiconductors.

2.3.1 Semiconductor basics

The main result from the nearly-free electron model showed that the electronic band structure in a crystal solid is divided into allowed energy bands and gaps which has no available energy states. A semiconductor can be defined as a solid where the density of available states is zero at the chemical potential at $T = 0$ K [15]. This means that one of the energy bands is completely filled, while the higher bands are empty. The occupied band is called the *valence band*, while the empty band is called the *conduction band*. Electrons residing in the valence band are unable to be excited into higher energy states by an amount less than the energy difference of the bands, known as the band gap energy. At finite temperature, we have seen that the Fermi-Dirac distribution develops a so-called *soft zone* around the Fermi level, giving a finite probability of some states above the Fermi level to be occupied (as shown in Figure 2.2). The soft zone is approximately 100 meV wide at room temperature. Band gaps of most intrinsic semiconductors are much larger than this, but typically less than 3 eV [15, 32].

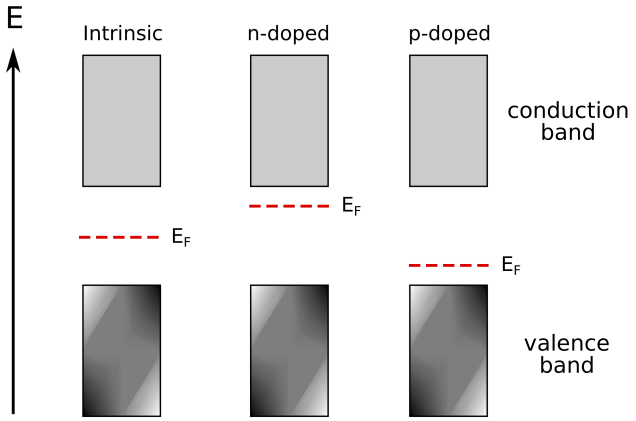

Figure 2.5: Doping of semiconductors. The Fermi level can be shifted by doping the intrinsic semiconductor with impurities having either additional (n-type) or less (p-type) valence electrons.

The configuration of the energy states around the band gap can be altered by *doping* the semiconductor. The process of doping relies on the introduction

of new states within the band gap, effectively changing the chemical potential of the material. This concept is fundamental to semiconductor devices and has been extensively exploited in electronic technology for the past decades. Doping is achieved by introducing impurities to the semiconductor lattice, either having one more or one less electron per atom than the host material. This is known as n-type and p-type doping, respectively. n-type doping give rise to new states below the conduction band, raising the Fermi level. p-type doping create available states near the valence band band, lowering the Fermi level. This is illustrated in Figure 2.5. Doping can dramatically change the electronic properties of the semiconductor, as there now exist loosely bound electrons that can be easily excited by small energies.

2.3.2 Fundamental properties of silicon

Silicon (Si, atomic number 14) is a type-IV semiconductor with a diamond crystal structure, consisting of covalent bonds between four sp^3-hybridized orbitals. The crystal can be described by a fcc Bravais lattice with two atoms in the basis; one at (000) and the other at $(\frac{a}{4}\frac{a}{4}\frac{a}{4})$ along the body diagonal, where $a = 5.431$ Å is the Si lattice parameter [15, 32]. Due to its Bravais lattice, crystalline Si has a cubic symmetry [38]. The 3D Brillouin zone (BZ) is a bcc Wigner-Seitz cell [38] (see Figure 2.6).

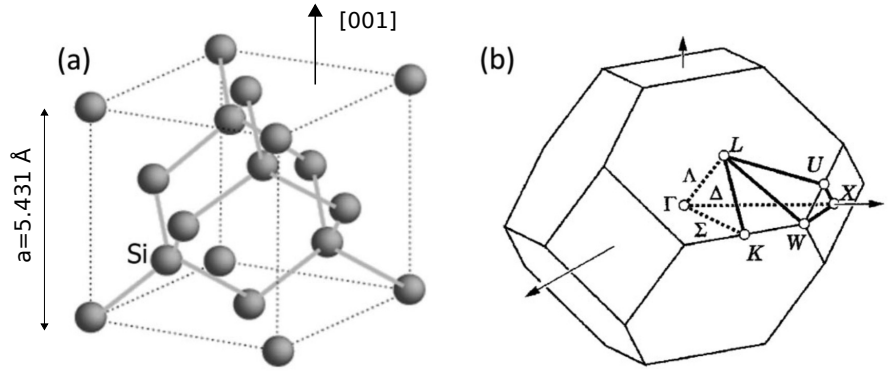

Figure 2.6: Bulk Si crystal structure in real and reciprocal space. (a) Real space unit cell. The diamond structure is described by the face-centered cubic Bravais lattice. (b) Body-centered cubic Wigner-Seitz cell in reciprocal space, describing the first Brillouin zone. Adapted and reprinted from Ref. [38].

Figure 2.7 shows the electronic band structure of bulk Si along two directions in reciprocal space. We see that Si has a band minima towards the Brillouin zone boundary near the high symmetry X-point, giving an indirect band gap of

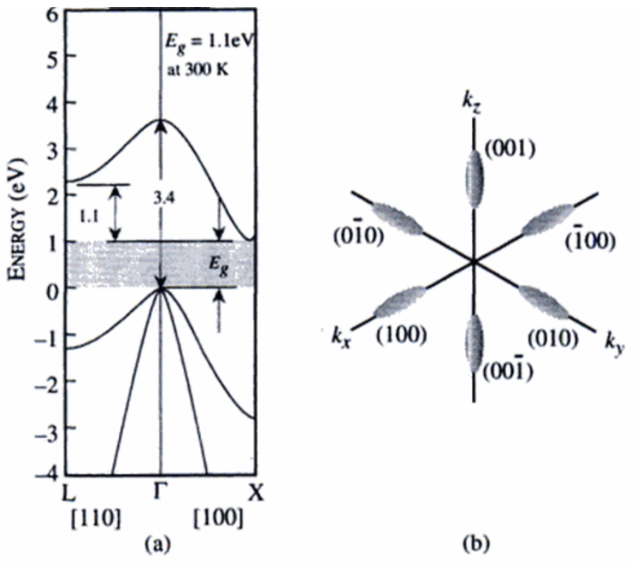

Figure 2.7: Band structure of bulk Si and Brillouin zone locations of the conduction band minima. (a) Bulk band structure of Si at 300 K along the $L-\Gamma-X$-directions of the Brillouin zone. The indirect bandgap is shown (shaded). (b) Brillouin zone locations of the six degenerate valleys of the bulk Si conduction band minima. Reprinted from Ref. [32].

approximately 1.12 eV at 300 K [32]. Due to the symmetry of the reciprocal lattice the conduction band minima has a six-fold degeneracy in reciprocal space [38]. This is illustrated by Figure 2.7(b).

2.3.3 δ-doping

Phosphorus (P, atomic number 15) has five valence electrons compared to four in Si, making it a n-type dopant. Thus, P doping of Si[4] will raise the Fermi energy compared to the bulk Si crystal. A narrow, heavily phosphorus-doped region encapsulated in a bulk Si crystal is known as a *Si:P δ-layer*. The most extreme configuration is the *monolayer* (ML), which consist of an atomically sharp dopant profile. The thickness can be increased to several atomic layers, but the monolayer is the most extensively studied due to its increased relevance for device applications. The density of dopants in the δ-layer will vary depending on the method of fabrication, but calculations typically operate with a 25% dopant density (normal saturation, see e.g. [8, 22]). This will be discussed in greater detail in later chapters. The sharp dopant profile of the δ-layer creates a discrete chemical potential due to the raised Fermi level, which is not a stable configuration. Electrons will

[4]Not to be confused with p-doped Si, referring to a p-type dopant.

flow from the doped region, ionizing the donors to create a net positive charge in the dopant layer. The resulting electric field will counteract the Fermi level step to produce a constant chemical potential throughout the solid at thermal equilibrium. As a result, the conduction band will bend, creating a potential well in the region of the δ-layer. If the doping profile is sharp and dense enough, the depth of the well will cross the Fermi level, creating a strong confinement in the direction perpendicular to the δ-layer. As a consequence, new available states in the Si band gap will make the dopant region metallic [24]. The confinement effects will break the degeneracy of the conduction band minima, creating discrete, highly localized energy states. In effect, this is a quantum well, confining electrons in the δ-layer to in-plane movement in a two-dimensional electron gas (2DEG). Generally, a higher dopant density is shown to increase the confinement [22]. A calculated confining potential profile is shown in Figure 2.8. The three lowest energy states of this quantum well system are named 1Γ, 2Γ and 1Δ, and represent the main subject of interest in this thesis.

The two dimensional character of the layer leads to a collapse of dimensionality of the Brillouin zone, where the 3D BZ is projected onto a 2D sheet. This can be seen in Figure 2.9. As a consequence, the out-of-plane locations of the conduction band minima (along the k_z-direction in Figure 2.7) is projected down to the 2D Brillouin zone center Γ-point, while the other four locations are projected to their own positions. The out-of-pane locations give rise to the 1Γ and 2Γ states, while the 1Δ-states are associated with the in-plane features [17, 27]. It is interesting to note that the Brillouin zone projection leads to equivalent locations in the 2D BZ not necessarily corresponding to the same 3D BZ location. This can be seen by traversing between neighboring 2D zones in two different directions (red and green arrows of Figure 2.9). The consequences of this is vital to understanding the photoemission process of such states, as we shall see in later chapters.

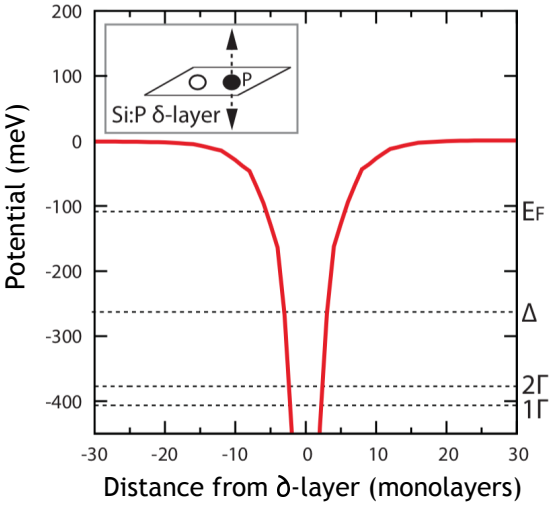

Figure 2.8: Calculated Si:P δ-layer potential profile. Result of tight-binding calculations on a monolayer δ-layer of 25% dopant density. Predicted minima of 1Γ, 2Γ and 1Δ states are indicated. Reprinted from Ref. [22].

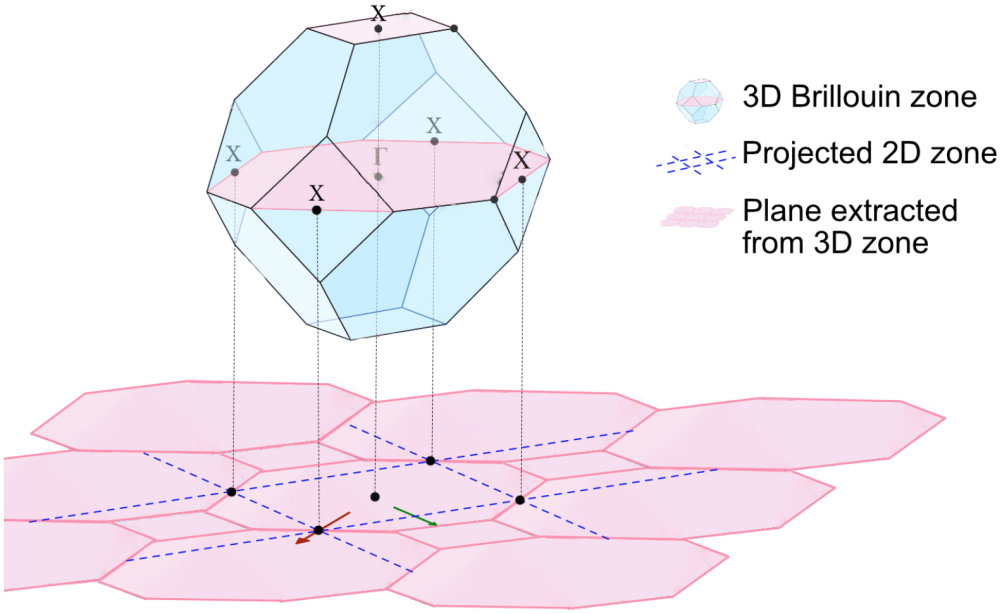

Figure 2.9: Brillouin zone projection from 3D to 2D. Four in-plane X high-symmetry points of the 3D Brilouin zone (BZ) are projected to the corners of the 2D BZ, while two out-of-plane X-points are projected to the 2D zone center (Γ-point). Note that the projected 3D plane leads to neighboring 2D Brillouin zones not necessarily representing the same regions of the 3D BZ (illustrated by traversing from one 2D zone to the next along the green arrow compared to along the red arrow). Reprinted from Ref. [17].

2.4 Existing work

Si:P δ-layer structures have been extensively studied by various numerical models to predict several key properties of these systems. This includes density functional theory (DFT), tight-binding (TB) and effective mass theory (EMT) approaches [10, 11, 22, 24, 27]. Particurlary, the effects of the dopant configuration in the layer have been of interest. Tight-binding calculations of the electronic band structure of an ideally doped Si:P monolayer system as well as the impact of changing the dopant density on the band minima is shown in Figure 2.10. The corresponding potential shape is shown in Figure 2.8. We see that both the 1Γ, 2Γ and 1Δ states are predicted to reside below the Fermi level. By observing the curvature of the predicted bands we see that the valleys of the Γ and 1Δ states can be associated with different effective masses of the bulk Si band minima; the Γ states with the transverse effective mass ($m_T = 0.19m_e$) and the 1Δ states with the longitudinal effective mass ($m_L = 0.98m_e$) [10, 28].

The Γ states have been studied and verified experimentally in several articles

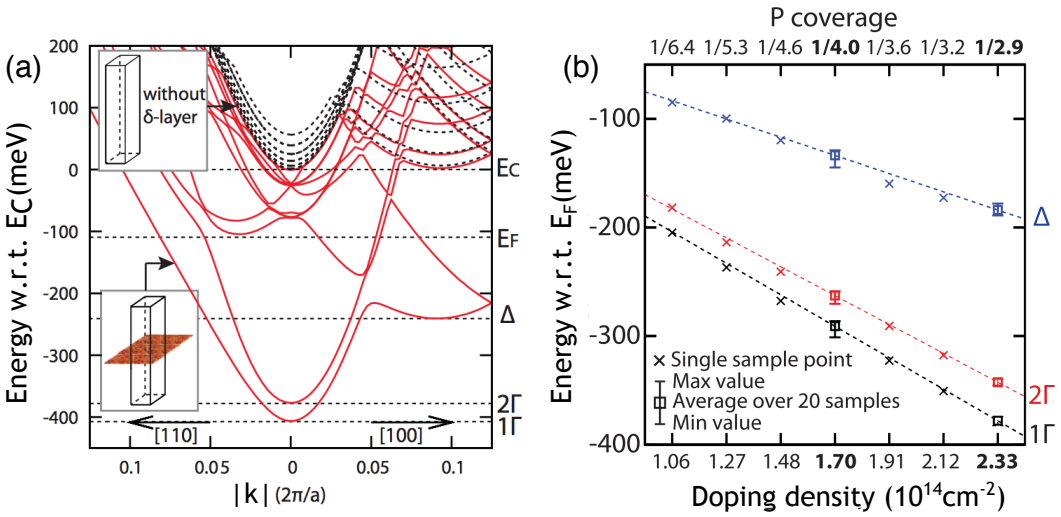

Figure 2.10: Tight-binding calculations of a Si:P monolayer doping profile. (a) Modified band structure of an ideal ordered δ-layer of 25% dopant density (red lines) along two directions parallel to the layer. The energy minima of the three lowest energy states of the quantum well (the 1Γ, 2Γ and 1Δ) are indicated. Bulk band states are shown for reference (dashed black lines). Energies are given with respect to the conduction band minima. Calculated valley minimas of the 1Γ, 2Γ and 1Δ states as a function of dopant density. Energies are given with respect to the Fermi level. (b) Band valley minima for the δ-layer states as a function of dopant density. Adapted and reprinted from Ref. [22].

[24, 27, 28]. Still, the experimental findings deviate somewhat from the theoretical predictions. In particular, the observed difference between the 1Γ and 2Γ band minima, known as the *valley splitting*, is much larger than the calculated values (see Figure 2.11). The valley splitting is important for determining the electronic properties of the layer, and understanding how the splittings behave is of great interest to make use of these structures in atomic scale devices. Both calculations and experiments are sensitive to the arrangement of the dopants in the layer,[5] and this has been considered the main reason for the observed discrepancy (e.g. shown by DFT calculations in Ref. [28]). In an in-preparation article, Mazzola *et. al.* [25] present self-consistent tight-binding calculations that model the impact of changing the dielectric constant of the δ-layer on the band structure. Previously,

[5] It should be mentioned that tight-binding models are known for underestimating the magnitude of energy splittings, while DFT in general is considered more accurate. Still, DFT is more sensitive to the details of atomic arrangement used in the model.

the bulk Si value for the dielectric constant has been used for modeling the δ-layer properties. Results of these calculations show that a substantial increase in the dielectric constant produces an interesting effect that might explain the observed splittings (see Figure 2.12). In this case, another distinct band minima is brought down below the Fermi level at the Brillouin zone center, named the 3Γ. The predicted valley splitting between the 1Γ and the 3Γ is similar to that of the measured 1Γ-2Γ splitting. This could suggest that the measured band structure has been misunderstood in the past, and that the state previously referred to as 2Γ in measurements could instead be 3Γ, and that 1Γ and 2Γ have been mixed together in a common band, unresolved by measurements. However, I will continue to use the "old" terminology when referring to the Γ states throughout this text. In the discussion of the results, I will return to this topic to see how the presented data can supplement this conundrum.

For quite some time, the 1Δ states eluded experimental discovery, raising additional doubt around the validity of the projected band calculations and the predicted locations of the states. Recently, the states were observed in thicker δ-layer samples [17], but has not yet been observed in a monolayer. This thesis aims to contribute to the understanding of these systems by tracking the evolution of the states as the dopant layer is made thinner, going from bulk-like layers towards the atomically sharp monolayer. As we shall see, this will give a more nuanced picture on how the state splittings behave in the monolayer case, specifically by adding 1Δ state to the established experimental data.

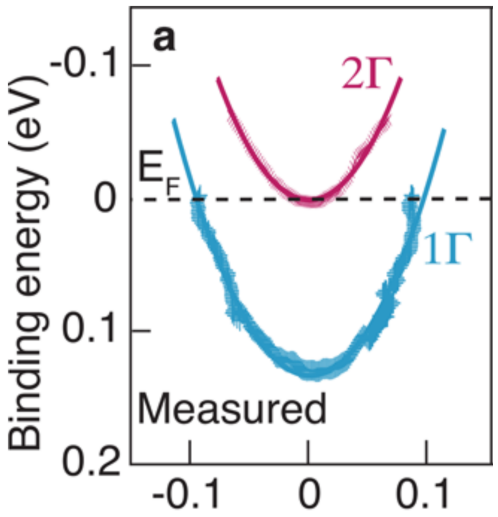

Figure 2.11: Measured band structure of a Si:P monolayer δ-layer. Parabolic bands (solid curves) are fitted to experimental data (crosses) to indicate the 1Γ (blue) and 2Γ (magenta) bands. Adapted and reprinted from Ref. [28].

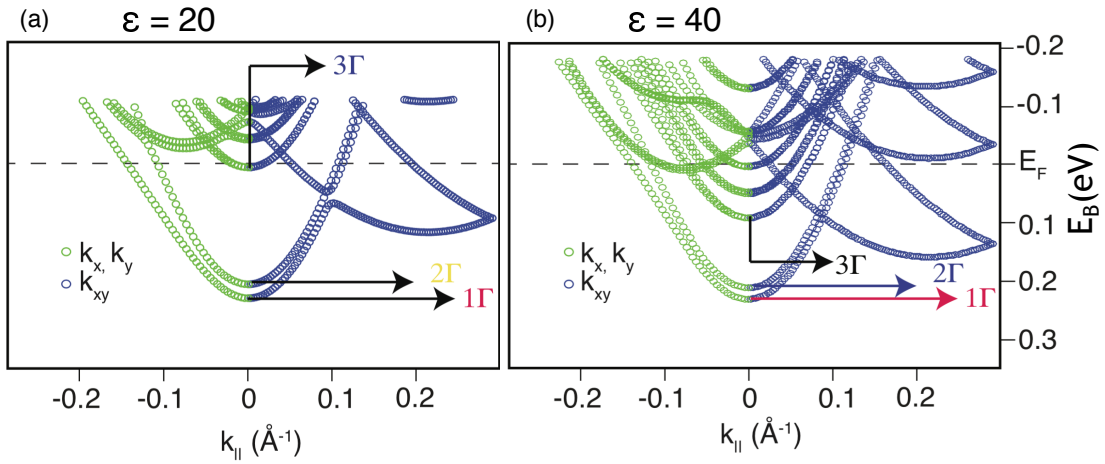

Figure 2.12: Tight-binding calculations of a Si:P 1/4 monolayer for different values of the dielectric constant ϵ. Modified band structure of the δ-layer for (a) $\epsilon = 20$ and (b) $\epsilon = 40$ along two directions of the Brillouin zone (k_x, k_y and k_{xy}). These values are increased compared to the bulk Si value ($\epsilon = 11.9$), which is assumed in the calculated structure seen in Fig. 2.10a). Valley minima of the 1Γ, 2Γ, 3Γ and 1Δ bands are indicated by arrows. Adapted and reprinted from Ref. [25].

Chapter 3

Experimental techniques and requirements

In this chapter I will cover the basic principles behind the experimental techniques used in the work of this thesis. This will include photoemission techniques to study δ-layer structures in Si, preparation techniques for making the structures, and some important practical requirements for carrying out the various parts of the process. Particular aspects relevant to the discussion of the experimental results is treated in greater detail.

3.1 Photoemission spectroscopy

3.1.1 Photoemission basics

Photoemission spectroscopy (PES) relies on the photoelectric effect to measure electrons emitted from a solid. Photons incident on a sample excite electrons in the solid by such an amount that the electron can overcome the work function of the material and escape into vacuum, where it can be observed by a detector. The short inelastic mean free path of electrons make PES techniques surface sensitive, probing only the uppermost nanometers of the solid [23]. Figure 3.1 illustrate the energetics of the photoemission process.

A photoemission event can be described in a simple picture through the *three step model*, which makes use of the same assumptions as the nearly-free electron model [9]. In the first step, electrons occupying an initial state in the solid are optically excited into an available Bloch-like bulk final state. Both energy and momentum must be conserved in this process. Conservation of energy is achieved simply by the electron absorbing the photon energy $h\nu$ and increasing its energy by an equal amount. For the momentum conservation however, the electron needs

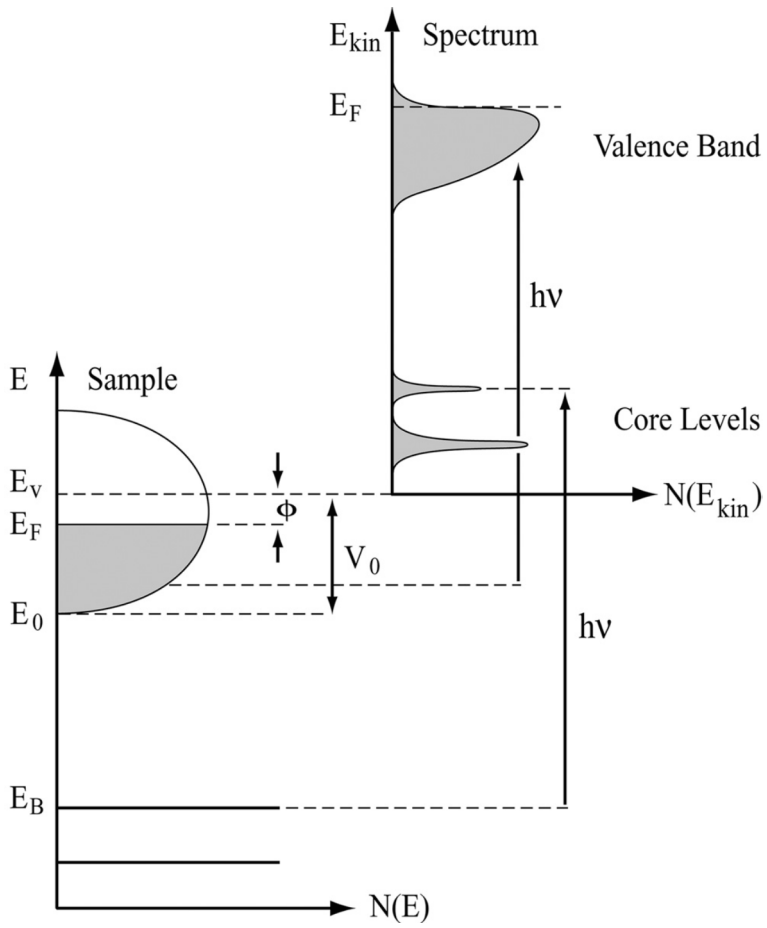

Figure 3.1: Energetics of a photoemission event. An electron is excited from an initial state by the energy $h\nu$ of an incident photon. The energy of the initial state can be found from the relation between the measured energy of the electron in vacuum (E_{kin}, relative to the vacuum energy E_V), the work function of the solid (Φ) and the photon energy. This produces a spectrum representing the occupied density of states in the solid (gray shading). Note the experimental broadening of the measured spectrum. Reprinted from Ref. [9].

help from the lattice, which provides the momentum in units of a reciprocal lattice vector $\mathbf{G}$. This corresponds to a vertical transition in the band structure, due to the fact that extended Brillouin zones are equivalent to the first Brillouin zone. This is illustrated in Figure 3.2. The momentum of the photon is very small, making it negligible for our purposes. In the second step of the model, the excited electron travels to the surface, and may be scattered elastically along the way according to its mean free path. In the final step, the electron escapes the surface via a matching

of the bulk state to a free-electron-like vacuum state, with a parabolic dispersion equal to the one presented in Eq. 2.3. The binding energy E_B of the electron state occupied by the electron before the photoemission event can be calculated from the observed kinetic energy in vacuum E_{kin}, the photon energy $h\nu$ and the work function of the solid Φ [9, 16] by the relation

$$|E_B| = h\nu - \Phi - E_{kin} \ . \tag{3.1}$$

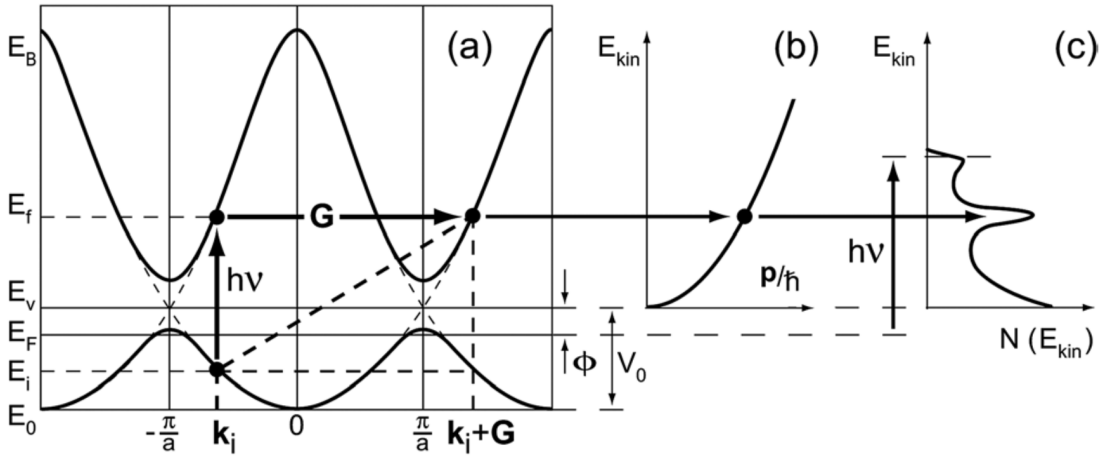

Figure 3.2: Kinematics of a photoemission event in the three-step model. (a) Nearly-free electron band structure, showing two Brillouin zones. Vertical arrow describes the first step in the model; the direct optical excitation of an electron from an initial state ($\mathbf{k}_i$, E_i) to a final state ($\mathbf{k}_i + \mathbf{G} = \mathbf{k}_i$, $E_f > E_V$). States are separated by the photon energy, conserving energy in the process. Momentum is conserved through the lattice supplying momentum in units of a reciprocal lattice vector $\mathbf{G}$, corresponding to a vertical transition in the first Brillouin zone. (b) At the surface, the final state matches with a free-electron state in vacuum and escapes the solid. (c) Measured spectrum of electron kinetic energy E_{kin} in vacuum, representing the density of occupied states (DOS) within the energy probing depth $h\nu - \Phi$, where Φ is the work function of the solid. Reprinted from Ref. [9].

The three-step model assumes that all three steps happen simultaneously, and that the solid left behind after the photoemission of an electron relaxes into a new state immediately in a discontinuous manner. Each step has an associated probability, and the total probability of a successful photoemission event is the product of the three probability factors [9].

There exists a range of photoemission techniques which make use of different photon sources and offer various functionalities. I will now present the details of

the specific photoemission technique used in this work, representing the means for investigating the electron states of the Si δ-layers.

3.1.2 ARPES

ARPES is short for angle-resolved photoemission spectroscopy, and is a powerful tool for measuring the occupied electronic band structure of metals and semiconductors [9, 16, 23]. The technique is also known as ARUPS (angle-resolved ultraviolet photoemission spectroscopy) due to the type of radiation used. The main idea behind this technique is to measure the direction and kinetic energy of photoemitted electrons and relate this to the original electron momentum and energy inside the solid. The instrumentation of an ARPES experiment can be seen in Figure 3.3. A photoemitted electron enters a hemispherical analyzer[1] which has a dispersive- and a non-dispersive plane with respect to the electron energy. In the dispersive plane, an applied voltage difference across the inner and outer parts of the hemisphere causes a bending of the electron trajectory which is dependent on the kinetic energy of the electrons passing through. Adjusting the applied potential makes it possible to control the energy range which passes the analyzer. In the non-dispersive plane, electrons are simply mapped according to their emission angle θ relative to the sample orientation (see Figure 3.3). The electron is then detected by a two-dimensional detector. The photoemission of several electrons give rise to a intensity distribution in the detector as a function of kinetic energy and emission angle.

Now, how can we use the measured quantities of the electron outside the solid to gain information about the original state of the electron? This is achieved by considering the conservation of energy and momentum at the surface. Energy is conserved, and the energy of the initial state can be found through the energetics of the photoemission process, given by Eq. 3.1. The conservation of momentum is a bit more complicated. The components of the outside momentum can easily be calculated from the geometry of the experiment. Due to translational symmetry at the at the surface parallel plane, the parallel momentum is conserved across the surface [9]. This makes it possible to express the electron initial state parallel momentum $k_{||}$ by known parameters:

$$k_{||} = |\mathbf{k}_{||}| = \frac{1}{\hbar}\sqrt{2mE_{kin}}sin\theta. \tag{3.2}$$

For the perpendicular momentum component $k_{\perp}$, the situation is different. This component is not conserved in the photoemission process, and there is no

[1] There are other ways of detecting electrons in a ARPES experiment, but I will only describe the case of the hemispherical analyzer.

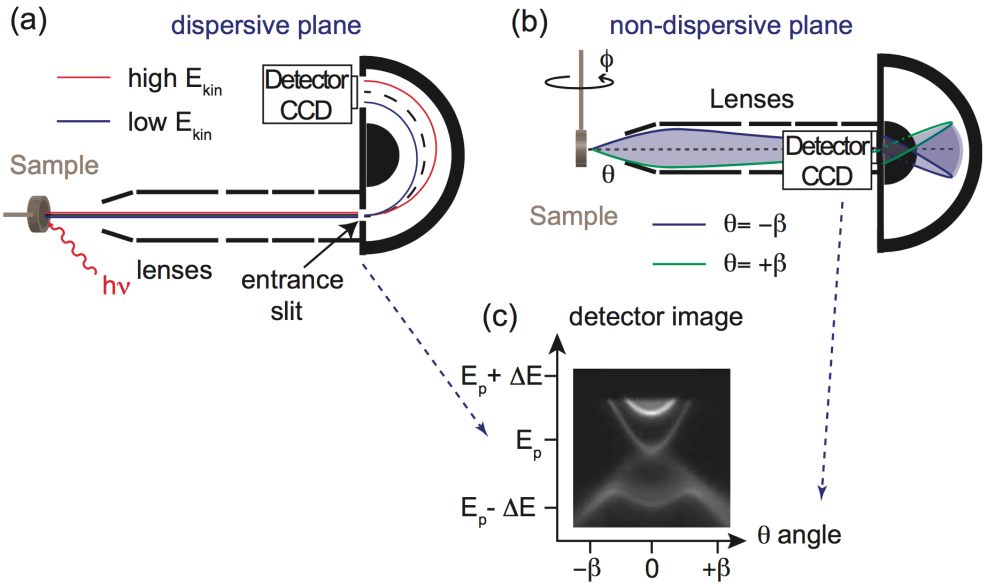

Figure 3.3: Instrumentation of angle-resolved photoemission spectroscopy (ARPES). (a) Cut through the dispersive plane of the hemispherical analyzer. Photoemitted electrons are deflected in a electric field set up between the inner and outer hemisphere. The dashed blue line represent the trajectory of electrons having an energy $E_{kin} = E_P$, called the pass energy. (b) Cut through the non-dispersive plane of the hemispherical analyzer. Electrons are mapped onto the detector according to their emission angle θ. (c) Resulting detector image. White contours correspond to higher detector intensity. Reprinted from Ref. [15].

way of telling the dispersion of the excited electron final state before the surface transmission. To solve this problem, an *a priori* assumption of final states is made. By assuming nearly-free electron final states, one obtains

$$k_\perp = |\mathbf{k}_\perp| = \frac{1}{\hbar}\sqrt{2m(E_{kin}cos^2\theta + V_0)}, \tag{3.3}$$

where V_0 is the *inner potential* of the solid, which can be calculated for a specific solid. Combining Eq. 3.2 and Eq. 3.3, we now have a way of relating measured quantities to the band structure of the occupied states $E(\mathbf{k})$ inside the solid. It should be noted that the non-conservation of the perpendicular momentum leads to a refraction effect across the surface. This effect is absent at normal emission and becomes more prominent as the perpendicular momentum component increases.

By varying the orientation of the sample and the photon energy, the dispersion-free plane of the detector will correspond to different cuts in reciprocal space, allowing the entire Brillouin zone to be mapped through multiple ARPES images.

Stacking these images produces a 4D data cube, allowing different slices to be extracted. Relevant to this text, an angle map refers to the slice in such a cube displaying the intensity distribution of a given energy for the emission angle θ versus the orientation angle Φ (see figure 3.3) which corresponds to two perpendicular directions in the Brillouin zone.

3.1.3 Imaging buried states

It can be difficult to imagine how one can measure the electronic states residing in a buried δ-layer using a highly surface sensitive technique such as ARPES. This is possible due to a resonant enhancment of the photoemission process, allowing the fraction of the δ-layer state wavefunctions that exists at the surface to be measured. This process has been studied and explained e.g. in Ref. [24] and Ref. [27]. The confined δ-layer-states have a two dimensional nature, i.e. they have no (or little) $k_\perp$-dependence. However, the photoemission of these states require coupling to bulk-like final states, which *do* depend on $k_\perp$. The photoemission process is therefore resonantly enhanced when particular regions of the Brillouin zone is probed, corresponding to the origin of the confined states. We have seen that the δ-layer-states that we wish to investigate originate from near the bulk BZ high-symmetry X-points. Resonance is therefore achieved when probing these regions of momentum space. The region that is probed will be related to the photon energy used and the orientation of the sample. For particular values of the photon energy, only certain values of $k_\perp$ lead to photoexcitation (see Figure 3.4). It must be noted that both the initial and final state have some broadening of $k_\perp$, meaning that the photoexcitation resonance may occur for a range of photon energies, but with different probabilities [24]. The work of this text relies on previously found ARPES parameters for the locations for the Γ- and 1Δ state resonances, given by Ref. [17, 27, 28].

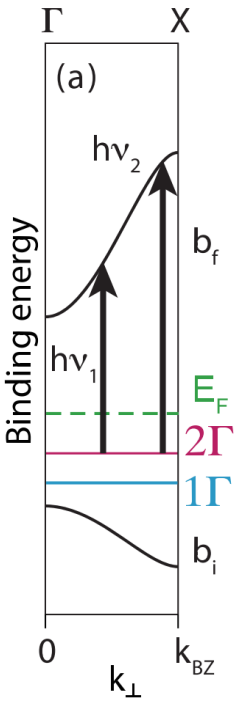

Figure 3.4: Photoemission resonance for the 1Γ and 2Γ δ-layer states. Only particular combinations of the photon energy $h\nu$ and the momentum component $k_\perp$ lead to photoemission. Reprinted from Ref. [24].

3.1.4 Synchrotron radiation

From the previous chapter, it is clear that we require great control over the Brillouin zone navigation during ARPES experiments to accurately measure the quantum well states

belonging to a δ-layer. For this, a variable photon energy
is crucial. This is achieved by using *synchrotron radiation*. A synchrotron generates electromagnetic radiation through the acceleration of ultra-relativistic charged particles around a storage ring using powerful magnets and insertion devices. The radiation is directed towards the experiment setup (called a *end-station*) via a so-called *beamline*, consisting of a series of mirrors and slits. The desired photon energy can be selected from a broad spectrum using a monochromator, which is a frequency filter using a spatial grating. Synchrotron-generated radiation has the advantage of being highly collimated and intense, allowing for very small bandwidths of the monochromator, greatly improving the energy resolution compared to other radiation sources. For more in-depth information on synchrotron radiation, the reader is referred to Ref. [5].

3.2 Ultra High Vacuum (UHV)

Silicon is very reactive, and surrounding particles will quickly stick to a clean Si surface causing contamination. It is therefore desirable to minimize the number of contaminant particles impinging on our sample. This is achieved by carrying out experiments inside a vacuum chamber. A vacuum environment with a pressure in the range of 10^{-9} mbar and below is known as *ultra high vacuum* (UHV), and is a key requirement for keeping samples clean for an extended period of time during surface sensitive experiments [16]. To achieve such an environment, particles are effectively removed from an enclosed system using a series of pumps. The gas inside the vacuum system is referred to as the *rest gas*, and is the working substance for the various pumps. The first step in the pumping process is a so-called *roughing pump*, typically a rotor-vane pump, which achieves a pressure of approximately 10^{-3} mbar. At this point, a turbomolecular pump (or simply just *turbo pump*) is utilized to further reduce the pressure. The turbo pump uses a stack of rapidly rotating blades which gives the rest gas molecules momentum in the direction of the roughing pump, which backs up the turbo. With this configuration, one can achieve pressures as low as 10^{-11} mbar. Once the pressure is reduced to a stable low value, an *ion pump* can be used to maintain the low pressure. This pump ionizes the rest gas molecules, which then sticks to a titanium cathode. The particles are thereby trapped in the pump so that they no longer can contribute to the chamber pressure.

The pressure in UHV systems is monitored by the use of specialized gauges. For pressures down to the $10^{\cdot 3}$ mbar range, a *Pirani gauge* is typically used. This gauge measures the pressure by sensing the current through a wire, in which the resistance is temperature-dependent. The wire temperature is again dependent on the amount of particles impinging on the wire, and thereby cooling it. The current

through the wire can then be calibrated to give a measure of the surrounding pressure. For lower pressures, an *ion gauge* can be used. Here, the rest gas is ionized by accelerated electrons in the gauge. The ions hit a wire, and the current through the wire becomes a measure of the rest gas pressure. Additional information on the vacuum environment can be achieved by using a mass spectrometer. The rest gas is ionized as in an ion gauge, and the ions are accelerated and filtered according to their mass-to-charge ratio before being focused onto a detector. This is an important tool for vacuum diagnostics, giving detailed information of the different species contributing to the chamber pressure.

Apart from the effectiveness of the pumps, achieving low vacuum pressure is affected by two main factors. The first one is by leaks. All ports and connection of a vacuum system may be the source of leakage, for instance from bad gaskets or flanges that are not tightened properly. The second factor is by the degassing of the vacuum chamber walls. This is mainly due to the evaporation of water molecules adsorbed on the surface, but the evaporation of other impurities also contribute. The degassing process will in principle happen by it self, but it takes a very long time to reach very low pressures. The process can be accelerated by *baking* the system, which means heating the system to approximately 200°C for an extended period of time. For additional information on the UHV principles and components measured above, see e.g. Chapter 3 of Ref. [16].

3.3 Preparation techniques

The aim of this section is to give a brief overview of the preparation techniques used in the experimental work of this thesis. The specific preparation schemes for preparing δ-layer structures is covered in the next chapter.

3.3.1 Sample heating

Annealing

In the previous section we saw how a UHV system represents a central requirement for keeping the samples that is to be investigated as clean as possible throughout the process. Inevitably, samples being brought into a UHV system from an atmospheric environment will be contaminated to some extent. This is especially true for Si due to its reactive nature, and consequently it has to be cleaned *in vacuo*. The process of *thermal annealing* is based on applying thermal energy to a system to either remove unwanted impurities or to improve ordering of crystal or surface structure [2, 23]. Si is well suited for surface cleaning by heating, due to the fact that its melting point is higher than the temperatures required to overcome the desorption energy of most contaminant species [16]. The annealing temperature

can be adjusted to achieve controlled desorption of selected chemical species. As an example, the native oxides of Si will desorb at approximately 600°C, while the lighter oxides require a lower temperature to come off. This can be utilized in the cleaning process, as the native oxides can help protect the Si surface from further contamination. A moderate temperature anneal for an extended period of time will allow light impurities to migrate from the bulk towards the sample and then desorb. This is referred to as *degassing*. A quick, high temperature anneal close to the sample melting point is called *flashing*, its purpose being to get rid of remaining, heavier contaminants. Annealing will also affect the crystal and surface structure. In the case of Si, surface reconstruction and surface defect formation is sensitive to the characteristics of the anneal. This will in turn will affect the chemical properties of the sample surface, making it an important parameter when preparing atomically sharp Si:P δ-layers [13].

Direct- and indirect heating

There are two main ways of heating a sample inside UHV; either by *direct-* or *indirect heating*. Direct heating use the resistive properties of the solid by applying a voltage across the sample such that a current is pushed through the material, thereby heating it. It is important to note that the resistive properties of the material being heated is temperature-dependent, meaning that the temperature increase is not linear with respect to the applied voltage. To avoid a sudden unwanted temperature increase, a current limiter can be used to gain some control. Direct heating does not work very well on insulators, and the method of indirect heating is then preferred. In this method a nearby filament (made by e.g. a tungsten wire) is heated, which in turn heats the sample.

3.3.2 Growth techniques

Thermal evaporation

The heating of materials is also the basis of the growth technique *thermal evaporation*. This is a easy and versatile way of growing thin films in a UHV environment. Thermal energy is added to a substance of a particular element, heating it to close to its melting point, causing it to evaporate. The substance can then condense on a nearby substrate surface, gradually forming a film. An Si evaporator device can be made by placing a piece of Si between two electrical contacts capable of delivering a high current through the material. The evaporator can be fitted on a port in a UHV chamber with electrical feedthroughs for connecting a power supply.

Gas dosing

Another useful way of growing a substance on a substrate *in situ*[2] is by gas dosing. In this case, the growth happens by chemical vapor deposition, where a gaseous element sticks to reactive surface sites of the substrate [36]. Gas is introduced into a UHV chamber via a leak valve, which are specifically designed for controlled gas admission to such systems. The dosing amount is measured by observing the pressure rise in the chamber as the gas is introduced. A mass spectrometer may be used to achieve greater control of the dosing process. In the work of this thesis, gas dosing was used to administer phosphine gas (PH_3) for the creation of the dopant layer. The reaction paths of PH_3 on Si is a complicated and much studied subject (see e.g. [13, 36, 37]). The main relevant reaction is the $PH_3 \rightarrow P + 3H$ dissociation encouraged by heating the sample, giving the possibility of separating the P from the H atoms in the δ-layer structure. Due to different desorption energies, a well suited anneal will remove the H atoms while the P atoms are incorporated into the Si crystal. This is central to the δ-layer sample preparation process, which will be presented in the following chapter.

[2] I.e. inside UHV without exposure to external environment.

Chapter 4

Experimental approach

This chapter will serve to document the experimental work conducted in relation to this thesis. This includes the instrumentation, the specific method of fabrication and data collection method through ARPES measurements. A brief discussion concerning the δ-layer preparation scheme is included to highlight some important aspects of the process.

4.1 Instrumentation

The data presented in this thesis was collected during two beamtimes at the SGM3 beamline of the ASTRID2 synchrotron facility, Center for Storage Ring Facilities (ISA) in Aarhus, Denmark. A picture of the beamline endstation used for the experiment can be seen in Figure 4.1. The samples were prepared and characterized *in situ*. Sample preparations was done in a dedicated silicon preparation chamber specifically designed for δ-layer growth, housing a Si evaporator and gas lines for phosphine gas dosing. The silicon preparation chamber held a base pressure of approximately $1 \cdot 10^{-10}$ mbar. The samples were heated by direct heating, and temperature readout was done by a mounted IR pyrometer. Evaporator and sample current control was achieved by two separate DC power supply units. ARPES measurements were carried out in the main analysis chamber, where the sample was mounted on a six-axis manipulator for total control of orientation. Photons were supplied by synchrotron radiation, with a selectable photon energy in the range of 12-150 eV. The setup allowed for ARPES measurements with an energy resolution better than 10 meV and angular resolution better than 0.1°[1] [6, 14].

[1] For a detailed schematic of the resolution of the beamline, see Appendix C.

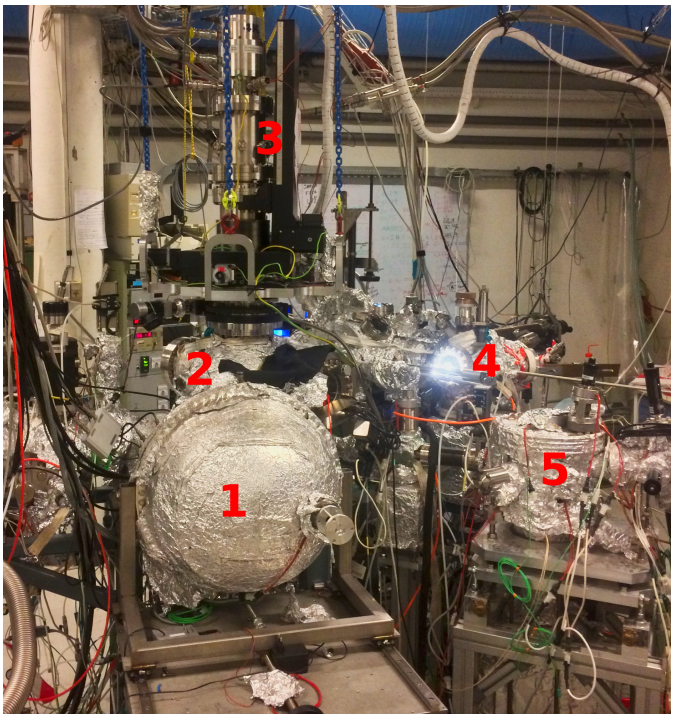

Figure 4.1: SGM-3 beamline endstation at the ASTRID2 synchrotron facility in Aarhus. Picture of the endstation used for sample preparation and ARPES characterization, showing 1) hemispherical analyzer (Specs Phoibos 150), 2) main analysis chamber, 3) main chamber six-axis manipulator, 4) dedicated silicon preparation chamber and 5) synchrotron beam entry from storage ring.

4.2 Sample preparation: δ-layer growth

Five samples with different δ-layer thickness were prepared. The layer parameters are shown in Table 4.1. The process started with a p-type (boron doped) Si(001) substrate which was cleaned in isopropanol (IPA) in an ultrasonic cleaner before being brought into UHV. All sample substrates were cut from the same Si wafer to minimize variations in sample properties. The sample was thermally cleaned *in vacuo* by degassing for at least 12 hours before being subjected to a series of thermal flashes. The number of consecutive flashes was determined by observing the pressure in the preparation chamber during the flashes. When the peak pressure during a flash was less than 10^{-9} mbar the sample was considered to be clean. After the final flash, the temperature was brought down slowly (≈ 2 °C/s) from 600°C to room temperature to achieve a well ordered, low-defect Si surface [13]. The sample was then held at room temperature for a minimum of 20 minutes before proceeding. The next step was the creation of the dopant layer. For the

Table 4.1: δ-layer thickness for the prepared samples. Estimated uncertainties can be found in Appendix A.1. The number of corresponding atomic layers for samples A-D is calculated from the crystal parameters of Si (see Section 2.3).

Sample ID	δ-layer thickness [nm]	Atomic layers
A	3	≈ 22
B	1	≈ 7
C	0.5	≈ 4
D	0.25	≈ 2
E	0.13	1 (ML)

monolayer sample, a double-dosing scheme was used. This was done to achieve a higher occupancy of the δ-layer states compared to a single dose scheme, which previously have shown to be insufficient to occupy the 1Δ states [17, 28]. PH_3 was dosed at $5 \cdot 10^{-9}$ mbar for 5 minutes to saturate the clean Si surface by sticking to the surface dangling bonds. After dosing the sample was annealed to desorb the H and incorporate the P atoms in the Si surface. This process was then repeated a second time. The double dosing approach is shown to produce dopant densities as high as 50% in the monolayer [26]. The growth of thicker layers was achieved through simultaneous dosing of PH_3 at $5 \cdot 10^{-9}$ mbar and thermal evaporation of Si at 0.4 Å/min[2] until the desired layer thickness was reached. The process is self-saturating, and is assumed to produce a dopant coverage of approximately 25% [26, 37]. The nature of the process leads to the continuous overgrowth of saturated dopant layers with Si, which then in turn is saturated by gas. To achieve saturation it is important that the partial PH_3-pressure is sufficiently high compared to the Si growth rate. To this end, the chamber pressure was monitored during the entire deposition to be able to observe any drop in PH_3 pressure, which then could be compensated for. After the deposition was complete, the sample was subjected to an incorporation anneal to cause the H to migrate to the surface and evaporate off, while incorporating the P atoms into the Si lattice. A capping layer of 1.5 nm Si was then deposited on the sample. This was done to increase the relevancy towards real device designs, which need be encapsulated because of the reactive nature of the materials involved. Finally, the sample was annealed to reconstruct the Si surface and promote crystal structure. The sample preparation process including details of the temperature and duration of the annealing steps is shown in Figure 4.2. Two different sets of anneal temperature parameters were used for the samples created at the two beamtimes. This is indicated by numbers

[2] The Si deposition rate was calibrated by XPS analysis of P 2p core levels during gradually Si encapsulation on a test sample. The details of this process is given in Appendix A.1.

(1) and (2) in Figure 4.2, applying to samples A-B and C-E, respectively.

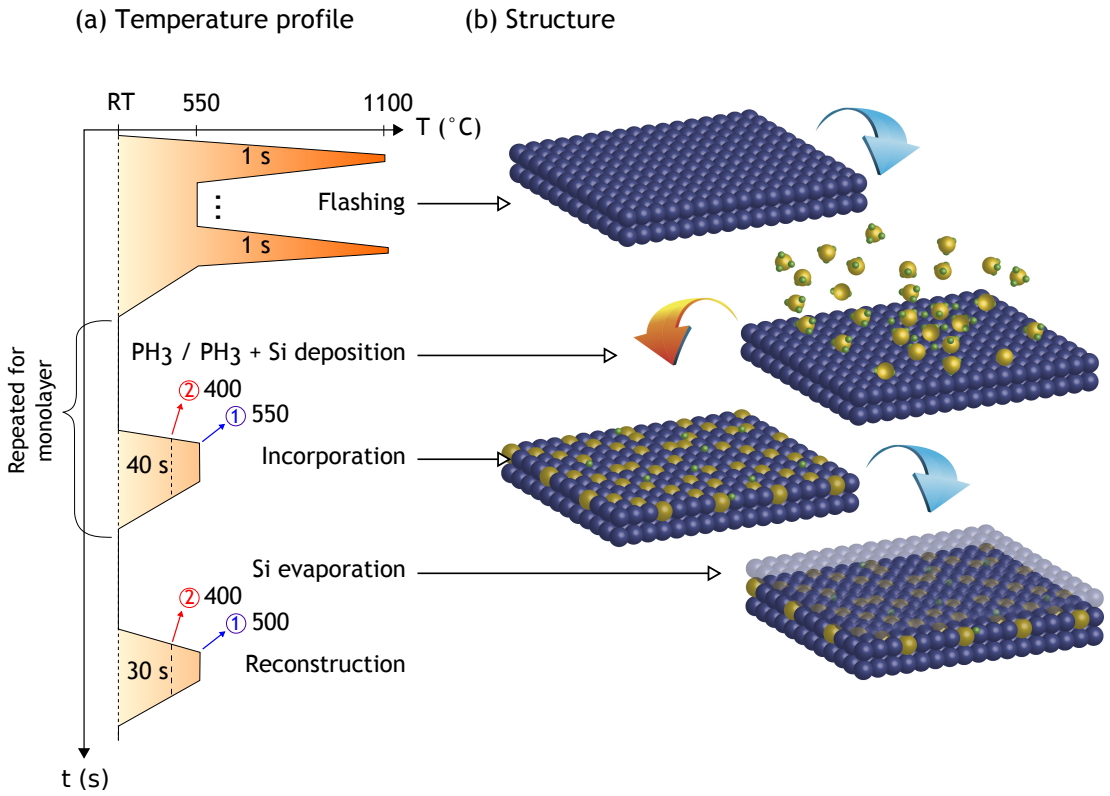

Figure 4.2: Schematic of the preparation process of Si:P δ-layer samples. Panel (a) shows the temperature profile of the annealing steps. The numbers 1 (blue) and 2 (red) indicate two different sets of temperature parameters used. Prior to this timeline the Si substrate sample was heated to 550°C for at least 12 hours (degassing) to remove most of the surface contaminant species through thermal desorption. The sample was then subject to a series of short, high-temperature thermal anneals (flashing) at 1100-1200°C to remove native oxides and remaining unwanted impurities on the surface. After the final flash, temperature was reduced slowly ($\approx$ 2°C/s) to achieve a well ordered, low-defect surface structure. The highly doped δ-layer was formed by dosing phosphine gas (PH_3) either by itself (monolayer growth) or by evaporating Si at the same time (thick layer growth). The sample was then annealed at 550/400°C for 40 seconds to remove H and to incorporate P into the silicon lattice. For the monolayer sample, the gas dosing and subsequent annealing step was repeated a second time to enhance dopant density (double dose). A capping layer of Si was then grown on top of the δ-layer, before reconstructing the surface with a final 30 second anneal at 500/400°C. Panel (b) shows the corresponding monolayer sample structure for each step of the process. The blue, yellow and green spheres represent Si, P and H atoms, respectively. Panel b) courtesy of Dr. Simon Cooil, used with kind permission.

4.3 ARPES measurements

Immediately after preparation, the samples were transferred to the main analysis chamber for ARPES characterization. First, the azimuthal rotation of the sample was calibrated to ensure correct orientation according to the desired Brillouin zone cuts. For this, a preliminary image of the Γ-states taken at its assumed location (at normal emission) was used. Definitions of momentum component directions and Brillouin zone locations of measurements are shown in Figure 6.2. A small, low resolution angle scan was collected at normal emission to find the precise location of the states. A detailed image of the Γ-states was acquired at the best location. A similar angle scan was then collected around the expected location of the 1Δ-state, and a detailed image was acquired at the best location. A Fermi surface was then produced by combining a series of images collected for different sample orientations. During measurements, the analysis chamber had a base pressure of approximately $2 \cdot 10^{-10}$ mbar, and the sample was kept at room temperature.

4.4 Comments to preparation scheme

Several variations of the monolayer growth scheme have been studied, e.g. through repeated dosing and annealing cycles and temperature variations [26, 37]. More complex stacking structures of dopant layers using silicon spacer layers and locking layers are also investigated [20, 21]. Variations in the preparation process are shown to be of great significance for the dopant properties of the layer. The growth of the thicker layers are less studied. When dealing with these structures, it is important to note that the processes involved are highly sensitive to the temperatures of the individual annealing steps. High temperatures can lead to dopant segregation (the migration of dopants out of the layer), effectively weakening the confining potential of the layer. This can also facilitate the formation of P-P dimers, causing electrical deactivation of dopants [20]. In the opposite case, too low temperatures can reduce the ordering of the lattice structures, or fail to remove unwanted species which can affect the layer configuration. The structure of the surface prior to dosing is also of great importance, particularly for the monolayer case. To approach the ideal dopant coverage and achieving the maximum number of active carriers it is crucial to produce a highly ordered, clean Si substrate surface [13]. Considering this, great care has to be taken when preparing these structures to ensure a consistent and precise growth.

Chapter 5

Numerical modelling

As we have previously seen, Si:P δ-layer structures have been studied through various numerical models to simulate variations in dopant properties in a monolayer configuration and its implications on the band structure (see Section 2.4). To my knowledge, the same is not true for the case of a varying δ-layer width. I will not attempt an elaborate treatment on par with the aforementioned calculations, as this is beyond the scope of this thesis. I will rather make use of a somewhat "naive" model to try and gain a quantitative picture of how the state valley splittings respond to a changing layer thickness. For this I will employ a simple 1D finite square potential well (as introduced in Section 2.2.4), giving a quantum mechanical treatment of the bound states residing in a narrow, confining potential. This is a much used model for semiconductor heterostructures, and should provide insight into some trends that can contribute to understanding the total behavior of a δ-layer system of varying layer width.

In this model, which I will simply refer to as the square well (SW) model, the δ-layer potential is approximated by a square potential well of width l and depth V_0 along the z-direction. The energy zero corresponds to the CBM of the bulk Si. The model is illustrated in Figure 5.1. From Section 2.4 we recall that the valley minima of the energy states we are concerned with can be associated with different effective masses. The implementation of this aspect will be key to predicting the behavior of the valley splittings in this simple model. The numerical task is now to solve the Schrödinger equation for bound states inside the well for different values of the width parameter l. The equation reads:

$$\left(-\frac{\hbar^2}{2m^*}\frac{d}{dz}^2 + V(z)\right)\Psi(z) = E\Psi(z). \tag{5.1}$$

Here, m^* is the effective mass and $V(z)$ is the square well potential shown in

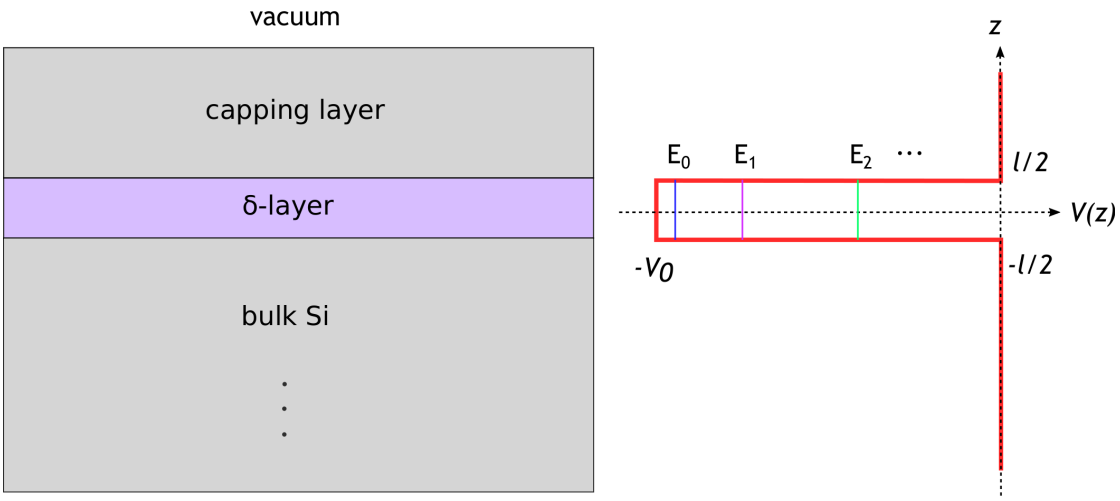

Figure 5.1: One-dimensional finite square well (SW) model of a δ-layer system. The potential set up by the δ-layer structure is approximated by a finite square potential profile $V(z)$ of width l and depth V_0. The energy eigenstates E_n of the bound quantum well states are found by solving the relevant Schrödinger equation for various values of the parameters l and V_0 numerically.

Figure 5.1. The energy eigenvalues are

$$E_i = \frac{\hbar^2 k_{z,i}^2}{2m^*}, \tag{5.2}$$

where the wave number k_z is quantized through the relations

$$\sqrt{\frac{2m^*V_0l^2}{\hbar^2} - (k_zl)^2} = k_zl\tan k_zl \qquad \text{(S)}, \tag{5.3}$$

$$\sqrt{\frac{2m^*V_0l^2}{\hbar^2} - (k_zl)^2} = k_zl\cot k_zl \qquad \text{(A)}, \tag{5.4}$$

for alternating symmetric (S) and asymmetric (A) wavefunction solutions of Eq. 5.1 [7]. The main output of the computation is the energy eigenvalues of the first two states having $m^* = m_T$ (bulk Si transverse effective mass, corresponding to the 1Γ and 2Γ states), and the ground state having $m^* = m_L$ (bulk Si longitudinal effective mass, corresponding to the 1Δ state). The valley splitting of the states are simulated for varying the well width and for different potential depths.

5.1 Accuracy of model - important shortcomings

If this model is to aid the understanding of experimental data, it is imperative that we have a clear notion of what this model can tell us - and what it can not. Before comparing to any actual data, we can already now address some important shortcomings of this model. First of all, by comparing the potential shape to previous calculations (Figure 2.8), it is evident that the square profile is not a very accurate approximation to the more Coulomb-shaped layer potential. In addition, the boundary conditions of the problem suggest that the potential is infinitely symmetric about the well center. This is not the case, as the width of the capping layer of overgrown Si is comparable to the layer thickness, especially for the thicker layers. Different potential shapes are expected to affect the energy eigenstates of the well, meaning that we can not expect the model to produce accurate predictions of the individual band minima. However, the purpose of the model is merely to give an impression of the overall trends of the state valley splittings, and for this the square potential is assumed to be a decent approximation.

It is important to note that this model will only give the contribution from the strongly quantized perpendicular momentum component k_z to the total energy of the bands. The model disregards that the states are in fact located at at different Brillouin zone sites, due to the projection of the zone from 3D to 2D (see Figure 2.9). Consequently, an energy offset is imposed due to the parallel component of the momentum $k_{||}$. The Γ states are located at the 2D zone center, while the 1Δ states are located towards the zone corners. If we assume that the total energy can be decomposed into factors dependent on the square of the momentum components (as is assumed in Ref. [10]), the 1Δ states should be shifted to higher energies to compensate for the larger $k_{||}$ component[1]. The exact amount will not be calculated in this thesis, as the trend of the splitting will come across regardless. For this reason, we will not pay too much attention to the energy scales in the calculated splittings, but rather concentrate on the overall trends that are produced.

5.2 Numerical results

Results of the numerical calculations from the SW model are shown in Figures 5.2 and 5.3.

[1] When the well is made wider, matters become increasingly complicated. As the states become more bulk-like, the Γ states will gain a non-zero $k_{||}$-component due to the reverse BZ projection from 2D back to 3D. This fact will be noted, but not accounted for in the numerical model.

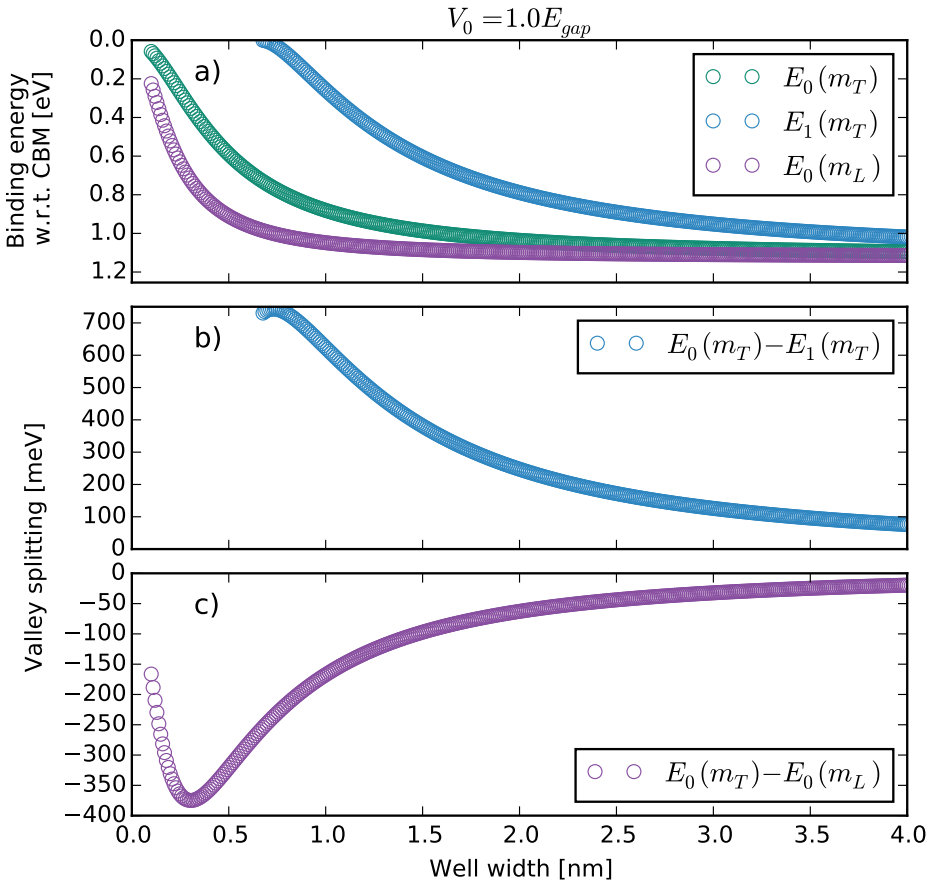

Figure 5.2: Numerical SW model - varying well width for different effective mass states. The well depth is set to equal the Si band gap. (a) Calculated binding energies with respect to the bulk conduction band minima for the ground- and first excited state for Si transverse effective mass $m_T = 0.21m_e$ (green and blue circles, respectively) and for the ground state for Si longitudinal effective mass $m_L = 0.92m_e$ (purple circles). (b) Calculated valley splitting between the ground state and first excited state for the transverse effective mass bands. (c) Calculated valley splitting between the ground state of transverse effective mass and the ground state of the longitudinal effective mass.

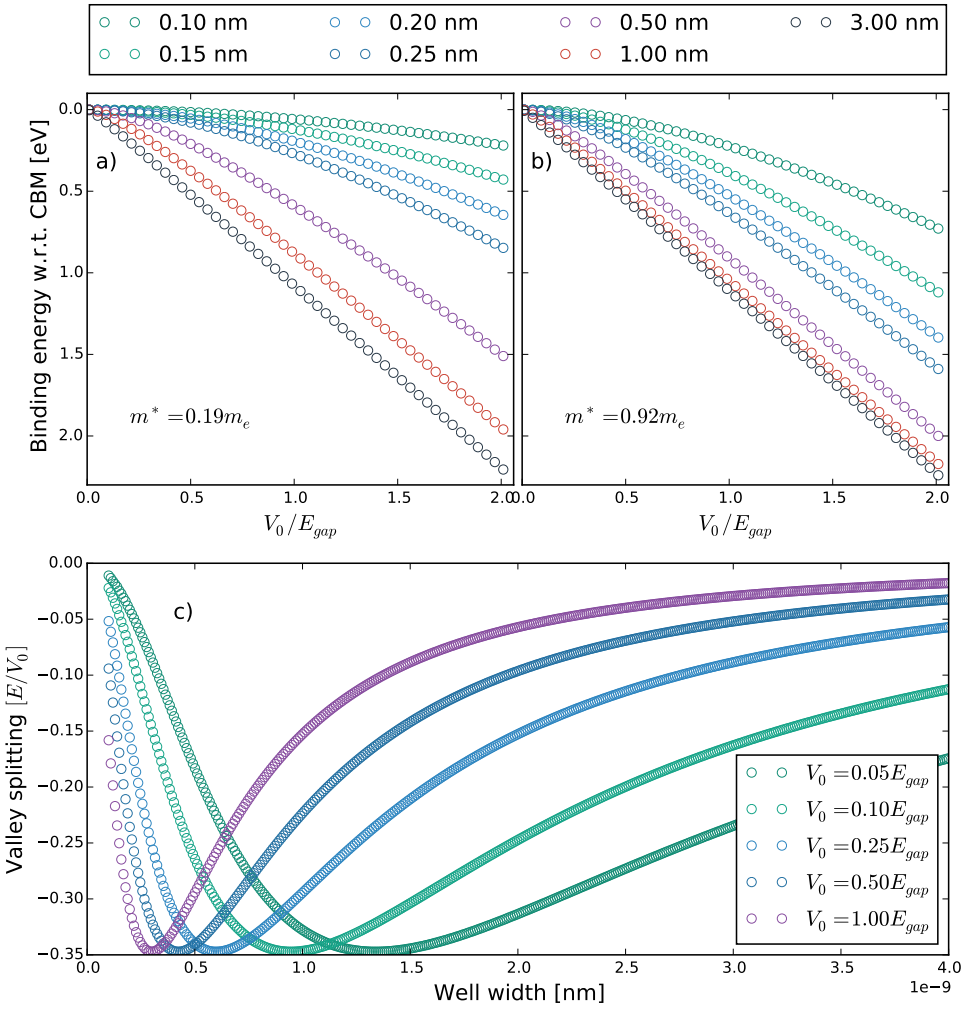

Figure 5.3: Numerical SW model - varying potential depth for different well widths and different effective mass states. The simulated response to varying the potential depth for the ground state energies of the transverse and longitudinal effective mass states are shown in panels (a) and (b), respectively. Different well widths are indicated by different color markers. Panel (c) show how the valley splitting between the two effective mass ground states are affected by changing the potential depth.

Chapter 6

Results, analysis and discussion

In this chapter I will present and discuss the experimental results collected in the work of this thesis. The purpose of the discussion will be to investigate how the energy states of the δ-layer respond to the changing layer thickness of the individual samples. Experimental broadening, signal noise and the Fermi level cutoff makes it difficult to point out the exact band structure in the measurements. Analyzing the results by data fitting is therefore fundamental to interpreting the data quantitively, enabling us to extract useful and accurate information on the electronic state dispersions. Therefore, I will start this chapter by looking at how the data fitting process was conducted. This will be central to the further discussion of some key aspects of the observed band structures. Following this, I will present Fermi surface measurements showing the observed location of the states and compare to previous work. Consequently, the measured and fitted bands of the individual states will be presented, before eventually treating the valley splitting trends of the states. The case of the monolayer will be treated in greater detail and compared to existing work.

6.1 Analysis and data fitting approach

The acquired ARPES data is subject to broadening both from the instrumentation and from the natural linewidth of the probed states. The broadening from the instrumentation is related to resolution effects, and can be modeled by a Gaussian profile. The natural linewidth arises from the uncertainty in energy and momentum of the states involved in the transition processes during photoemission, and can be approximated by a Lorentzian profile (see e.g. Ref. [35]). To incorporate

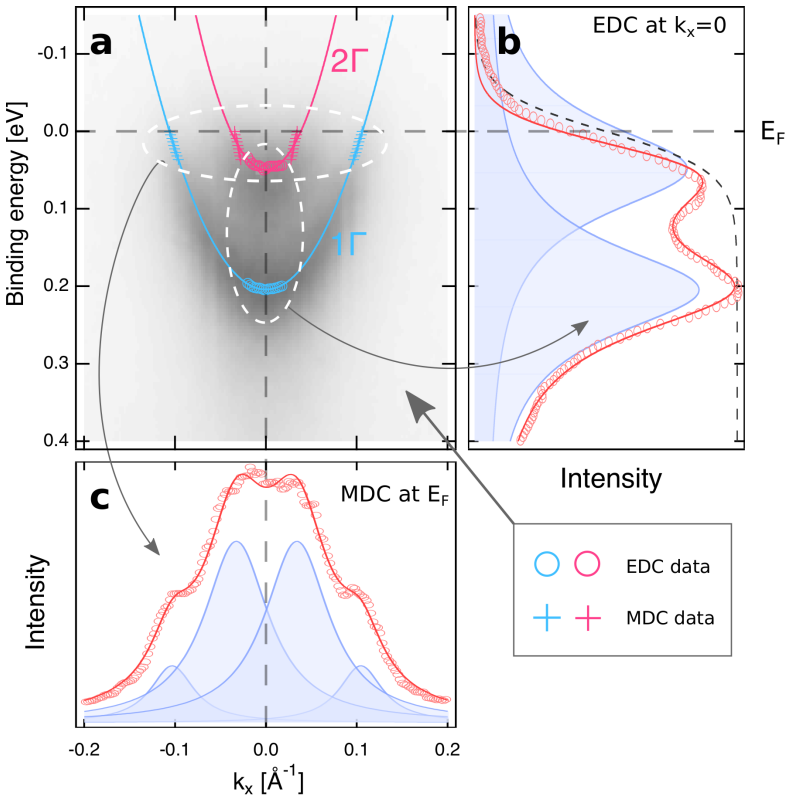

Figure 6.1: Illustration of data fitting process for δ-layer state ARPES data. (a) ARPES measurement showing 1Γ and 2Γ state bands. Darker features correspond to higher photoemission intensity. Several constant-momentum (EDC) and constant-energy (MDC) intensity distribution curves are extracted from the ARPES dataset. (b) Two Voigt profiles (blue) modulated by a Fermi-function (black dashed line) fitted against an EDC extracted at $k_x = 0$ (red line against red markers). (c) Four Voigt profiles fitted to a MDC taken at the Fermi level ($E_B = 0$). Parabolas are then fitted to the Voigt peak positions from all EDC and MDC fits (circles and crosses) to indicate the dispersion of the energy state bands (blue and pink curves in (a) for 1Γ and 2Γ, respectively).

both sources of broadening in the fitting process, a Voigt profile[1] was used as a fitting function. Since the measurement resolution in both momentum and energy given by the instrument used is better than the observed broadening, the Voigt profile was weighted towards a Lorentzian profile. The data fitting method is based on slicing the data set in two ways: 1) A constant momentum slice, giving

[1]A Voigt profile is a convolution between a Gaussian and a Lorentzian profile. True Voigt functions are very computationally expensive, so an approximated pseudo-Voigt profile was used, as provided by Igor Pro 7 software.

rise to a energy distribution curve (EDC), and 2) a constant energy slice, giving a momentum distribution curve (MDC). Several such slices were extracted from the ARPES data, before Voigt profiles were fitted to these curves. For the EDC case, a Fermi function at room temperature was included to modulate the Voigt profile across the Fermi level[2]. The peak positions of the fitted profiles in the various EDC and MDC slices were stored in a new data set, indicating points on a band with a momentum and a energy coordinate. Finally, parabolae were fitted against this dataset[3], to give the final fitted parabolic dispersion describing the energy bands. The process is illustrated in Figure 6.1.

Due to the purely mathematical nature of the fitting process, several assumptions had to be made to ensure that the outcome was physically reasonable. Further details on this matter as well as a brief discussion regarding the general quality of the fits and the associated peak position uncertainties is given in Appendix B.

6.2 Brillouin zone location of states

A measured Fermi surface of sample B (1 nm layer thickness) acquired with $h\nu =$ 118 eV is presented in Figure 6.2, along with a schematic illustrating the predicted location of the states relative to the 2D Brillouin zone. Equivalent maps were produced for the other samples. Even though the match is almost complete, we observe that the measured Fermi surface deviates from the prediction by containing only half of the 1Δ states. They seem to be missing one pair of "leaves" in each location of the Brillouin zone corners. To explain this, we recall the projection of the 3D bulk Brillouin zone onto a sheet describing the 2D Brillouin zone of the δ-layer (Figure 2.9). By comparing neighboring zones, we realize that even though we are probing equivalent regions of the 2D BZ, these projections actually originate from different regions of the 3D BZ. We have seen that the photoemission of these states depend on a resonant enhancement, coupling the initial 2D states to bulk final states. By considering panels (a) and (c) of Figure 6.2, we see that the leaves of the 1Δ states can be found in the corners of four neighboring 2D Brillouin zones which pairwise correspond to two different projected planes of the 3D BZ. We remember that the Γ-states originated from near the out-of-plane high symmetry X-points (i.e. the X-plane), while the 1Δ states were derived from the in-plane high symmetry points (i.e. the Γ-plane). Due to the resonance condition, the δ-layer states will be photoemitted through the bulk states corresponding to

[2]The location of the Fermi level was determined by integrating several EDCs over angular regions without occupied states and fitting a Fermi function. See Appendix B for further information.

[3]Parabolic dispersion of the δ-layer states is assumed, in accordance with previous work on the subject, as presented in Section 2.3.

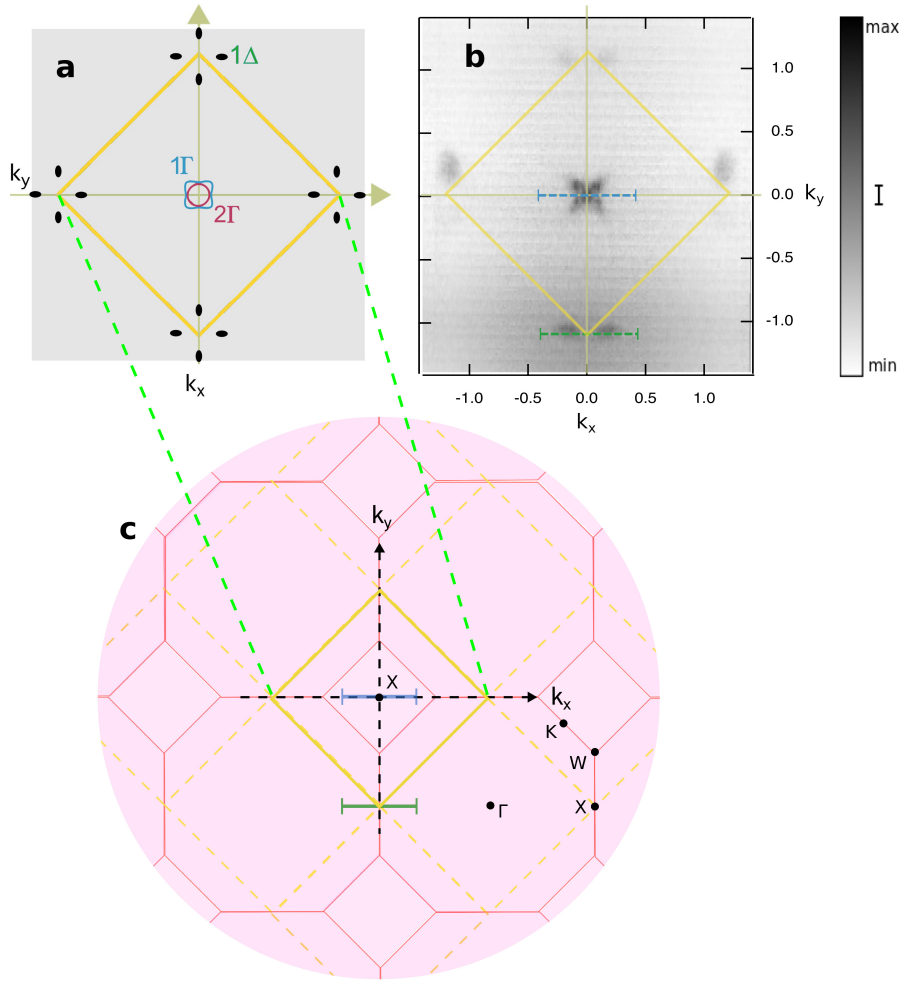

Figure 6.2: Predicted and measured Fermi surface (constant energy) showing locations of δ-layer states. The directions k_x and k_y correspond to the defined directions of the experiment. (a) Schematic of the predicted location of δ-layer states relative to the projected 2D Brillouin zone (yellow square). Reprinted from Ref. [17]. (b) ARPES Fermi surface measurement collected with $h\nu = 118$ eV, corresponding to near the X-plane of the bulk Brillouin zone. 2D Brillouin zone is overlain to facilitate comparison to (a). The blue and green dashed lines represent the momentum space regions probed for the Γ and 1Δ state ARPES measurements, respectively (Figures 6.3 and 6.5). (c) Brillouin zone projection showing neighboring 2D zones and corresponding 3D BZ locations. High symmetry points for bulk BZ are included for comparison to Figure 2.6. At the bottom corner of the center 2D BZ, a slice along the green dashed line traverses through regions corresponding to the bulk Brillouin zone Γ-plane, while a slice along the k_y axis traverses through regions corresponding to the bulk X-plane.

the 3D BZ location which is probed. This explains the missing leaves of the 1Δ states, as they pairwise will be resonantly enhanced by the parameters of the ARPES measurement. The opposite pair of leaves can be imaged by probing with a different photon energy and orientation of the sample, corresponding to a different cut in the $k_\perp$-direction of the bulk BZ (Γ-plane). An example of this can be seen in Ref. [17].

The measured Fermi surface confirms the existence and location of the states we are interested in. I will now continue to discuss the measured band dispersions of the δ-layer states. First, the fitted bands of the Γ and 1Δ states will be discussed separately, with the aim of highlighting some interesting properties of the systems. With this serving as a basis, the energy separation of the states as a function of the δ-layer thickness will be presented and compared to previous calculations and existing work.

6.3 Γ states

ARPES measurements of the different samples acquired at $k_y = 0.0$ Å^{-1} along the k_x-direction are shown in Figure 6.3. Fitted parabolae resulting from data analysis are overlain. There are particularly two points I wish to address from these results; the variation of the energy of the states, and the variation in observed intensity. The discussion of these results will serve to exemplify some key properties of the δ-layer parameters and how they affect the energy configuration of the system. This will be important considerations for discussing the energy splitting trends later on.

6.3.1 Energy variations

By considering Figure 6.3 we observe that the 1Γ band is shifted in energy for different sample dopant layer thickness. Comparing to the results from the numerical SW model, the observed behavior is surprising. Both ends of the width scale show a deviating behavior from the calculations. In the thinner samples, the expected rise of the band shifting towards lower binding energies as the layer is narrowed is completely absent. In the opposite end of the spectrum, the band actually shifts upwards in energy for the thickest samples. The observed deviations can be caused by a number of factors.

First, variations in the dopant properties of the different samples can contribute to explaining the observed behavior. I have previously presented calculations showing how the energy states of the δ-layer are directly related to the dopant properties (Figure 2.10b). We have also seen that the effects of dopant segregation and dopant density are highly dependent on the sample preparation process, which

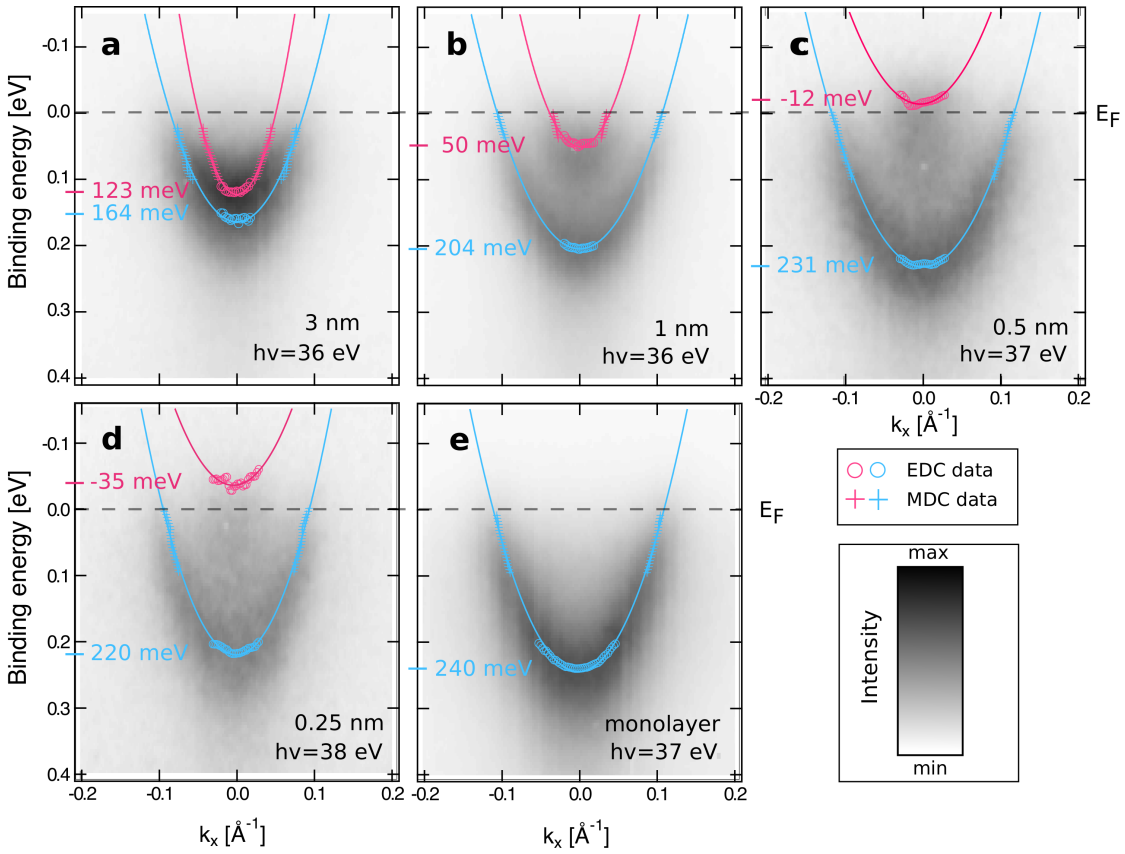

Figure 6.3: Measured Γ states band dispersion for various dopant layer thicknesses. ARPES measurements collected at $k_y = 0.0$ Å^{-1} for (a) 3 nm ($h\nu = 36$ eV), (b) 1 nm ($h\nu = 36$ eV), (c) 0.5 nm ($h\nu = 37$ eV), (d) 0.25 nm ($h\nu = 38$ eV) and (e) 1 monolayer ($h\nu = 37$ eV) Si:P δ-layer dopant profiles. Blue and magenta color correspond to the 1Γ and 2Γ states, respectively. Fitted EDC and MDC peak positions are indicated by markers, and fitted parabolae are overlain to show the location of the bands. The energies of the band minima are shown explicitly.

is prone to variations especially due to the delicate temperature dependence of the processes involved. The monolayer sample is the most evident case to be affected by this. Due to its alternative sample preparation scheme, it is expected to have a greater dopant density than the thicker layer samples. Calculations suggest a energy shift of $\sim$ 100 meV to higher binding energy for the 1Γ state for the assumed change in dopant density compared to normal saturation. This is seen as a major contribution to the observed behavior of the 1Γ state variation, as this will directly counteract the calculated confinement effects pushing the band upwards as the layer is made thinner. Dopant density variations may also be related to the upwards energy shift in the thicker samples. From the SW-model predictions presented in panels a) and b) of Figure 5.3, it can bee seen that the thicker samples appear to be more sensitive to changes in the potential than the thinner samples. This could mean that some energy shift in the thicker layers might be ascribed to dopant properties, even for small changes in the dopant configuration. If this is the case, it suggests that a lower dopant density has been achieved in the two thickest samples. This can be seen as a result of the larger incorporation anneal temperatures used for these samples, promoting dopant segregation and diffusion. This is consistent with the considerations of the preparation scheme presented in Chapter 4.2.

It is not considered likely that changes in the dopant density alone can explain the observed 1Γ behavior for the thinner samples. The approximations made in the SW model are also expected to contribute to the observed discrepancy. In the previous chapter, I addressed how the assumption of a square potential could significantly change the confinement of the states in the well compared to a more accurate potential shape. This means it is possible that the model falsely predicts the magnitude of the raising of the energy levels as a result of the potential approximation. This is assumed to be a significant effect. Another contributing factor could be a charge redistribution due to the change in the number of bands that are contributing to the electronic properties of the layer. As the 2Γ state disappears above the Fermi level, a lot of electron states are made unavailable. If some of the electrons previously occupying the 2Γ band were to migrate to the 1Γ band, this would lead to a lowering in energy, counteracting the reduced width effect. The charge redistribution effect is explained in greater detail by Ref. [17].

It should also be noted that some of the presented measurements for the different samples are acquired with different photon energies. This could in principle affect the energy of the states, as different photon energies will correspond to different cuts of the BZ through varying the $k_\perp$ momentum component (see Section 3.1.2). For states dispersing with $k_\perp$, i.e. states that have some 3D character, this means that we might not be sampling the true minima of the states. Investigations of the 1Γ state energy minima as a function of photon energy were

conducted, suggesting that a photon energy of 37 eV is most favorable for probing the true valley minima of this state. However, the difference in valley minima for 36, 37 and 38 eV was not found to be significant. In fact, for the thinnest samples there was no apparent difference. This is because of the states being of a 2D character with little or no $k_\perp$-dependence. For the thicker layers the difference was found to be within the experimental- and fitting uncertainty. For this reason, the ARPES data is presented for the photon energy corresponding to the highest quality measurements, making the data fitting more reliable.

Let us now consider the 2Γ state variation. As the layer is made thinner, the 2Γ is pushed above the Fermi level, making it hard to predict the energy of the band accurately. Still, making some assumptions about the relationship to the 1Γ state makes it possible to include a peak describing the 2Γ valley in the EDC fits. This is the case for the 0.5 nm and 0.25 nm samples, shown in panels 6.3c) and 6.3d), respectively. While doing this, one must keep in mind that the intensity relation between the two states is not straightforward to predict, a matter I will return to in the next section. I found that fitting with the assumption of a reasonably wide valley splitting interval, putting the 2Γ above the Fermi level, as well as imposing a common width parameter for the two Γ states, improved the fit of the single peak below the Fermi level significantly. Nevertheless, the 2Γ peak positions of these two samples are related to a larger uncertainty than the directly observed bands. For the monolayer sample there is no basis for fitting the location of the 2Γ band, as the data show no evidence of the tail of the band coming down below the Fermi level. We have previously seen that the width of the Fermi-Dirac soft zone is approximately 100 meV at room temperature. Taking into account the broadening of the state, we can make the assumption that the state must lie at least 50 meV above the Fermi level. The 2Γ data point for the monolayer in Figure 6.6 is thus based on this assumption. This will be important to keep in mind for later discussion.

6.3.2 Intensity variations and resonant enhancement

It is interesting to observe the measured intensity of the 1Γ and 2Γ states relative to each other. In the thickest sample (3 nm layer, Fig. 6.3a), the 2Γ is clearly the most intense, and analysis show a near 4:1 ratio of the fitted EDC peak areas in the slice extracted at $k_x = 0.0$ Å^{-1} . In comparison, the sample having a 1 nm layer (Fig. 6.3b) show a much more even intensity relation between the two bands. One explanation for this is that the Fermi slope attenuates the signal of the bands at low binding energies. Considering the width of the Fermi soft zone, some attenuation can be credited to this effect. Still, my analysis show that this can not account for any significant intensity reduction of the 2Γ band minima at $k_x = 0.0$ Å^{-1} . MDC data clearly indicate that the band minima lies below the Fermi level

(see e.g. Figure 6.1), so the explanation of the signal being a tail of a higher state can also be discredited. Instead, we must return once more to the physics of the photoemission process to give a reasonable explanation for the observed phenomenon. To achieve resonant photoemission of the states, only certain values of the photon energy will couple a initial state to a final state through which it can be photoemitted. Since the Γ states are separated in energy (at least for sufficiently

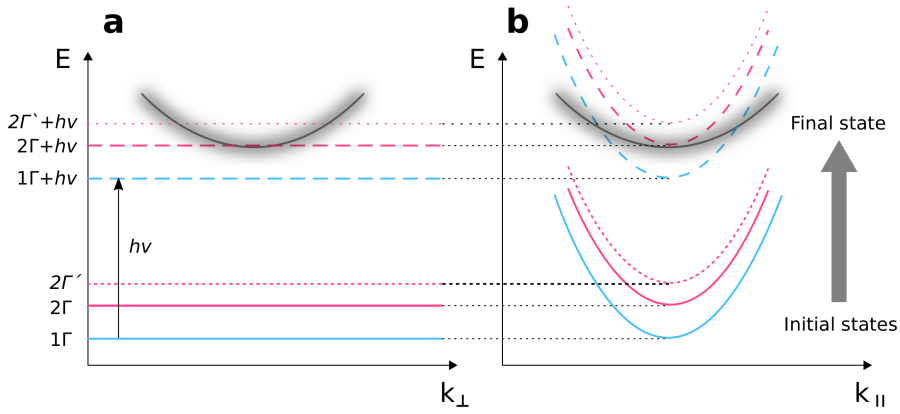

Figure 6.4: Photoemission resonance for Γ-states. Photoemission occurs when an initial state couples to a final state via excitation of an amount equal to the photon energy $h\nu$. Momentum conservation must also be considered, limiting the possible values of the momentum components. (a) Situations for a given $k_{||}$ (a) and $k_{\perp}$ (b) is shown. Assuming true two-dimensional δ-layer states, the Γ-states exhibit no dependence on the perpendicular momentum. In the depicted situation, the 2Γ state is in resonance and appears more intense when imaged by ARPES. The resonance condition changes as the state is moved up in energy ($2\Gamma'$). The blurred line of the final state illustrates that the resonant condition is fulfilled for a range of momentum values, as both initial states and final states are subject to some broadening. It should be noted that the thicker samples are not completely two dimensional, and will exhibit some $k_{\perp}$-dependence. This will lead to some initial state dispersion with $k_{\perp}$.

confined systems), which state is favored to be resonantly enhanced will depend on the parameters of the measurement and the dispersion of the states involved. This is illustrated in Figure 6.4. For the 3 nm sample, we can interpret the situation as the 2Γ state being in a more favorable position for the resonant condition than the 1Γ. Since both the initial states and the final state is broadened to some degree, the 1Γ state, found at a higher binding energy, is still photoemitted, but with a lower associated probability. Thus, the 2Γ appears more intense than the 1Γ. For the 1 nm sample, the situation is different. Now, the 2Γ state has moved to a lower binding energy, effectively weakening the resonance condition of the state. The 1Γ is found at a slightly higher binding energy, but still comparable to the

thick sample band. The result is that the two states couple to the final state with a similar photoemission probability.

6.4 1Δ states

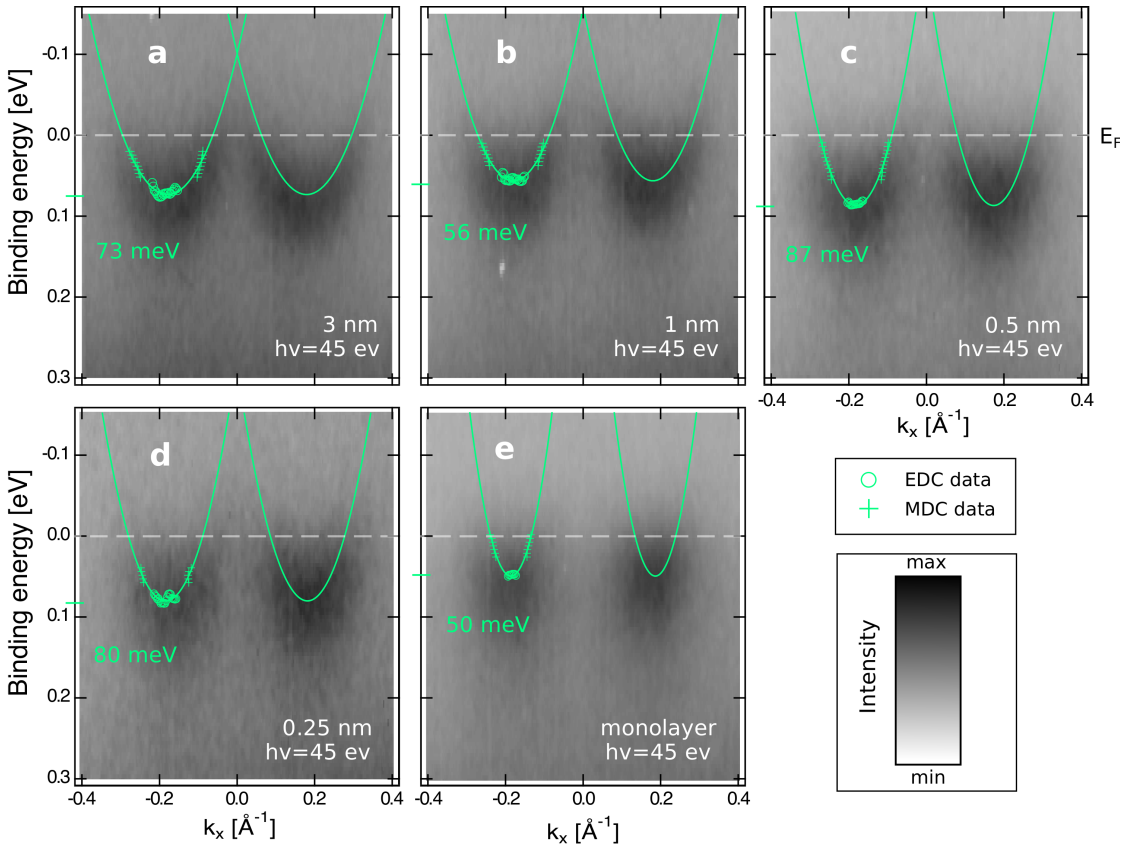

Figure 6.5: Measured 1Δ states band dispersion for various dopant layer thicknesses. ARPES measurements acquired with $h\nu$ = 45 eV at k_y = 1.1 Å^{-1} for (a) 3 nm, (b) 1 nm, (c) 0.5 nm, (d) 0.25 nm and (e) one monolayer thick Si:P δ-layer dopant profiles. Fitted EDC and MDC peak positions are indicated by markers, and fitted parabolae are overlain to show the location of the energy bands. The energies of the band minima are shown explicitly.

ARPES measurements showing the bands of the 1Δ states for the different samples is presented in Figure 6.5, acquired with $h\nu$ = 45 eV at k_y = 1.1 Å^{-1} along the k_x-direction. The left band was used for data fitting, and the results are overlain on both bands by mirroring about $k_x = 0.0$ Å^{-1} . Panel e) shows, for the first time, experimental evidence of the 1Δ state in a true monolayer δ-layer.

The 1Δ state measurements have a lower signal-to-noise ratio compared to the Γ state measurements, making it harder to obtain accurate fitting data. At first glance, this could indicate that the 1Δ states are less occupied than the Γ states, contradicting calculations presented e.g. in Ref. [10]. One must however be careful to draw this conclusion. The photoemission process complex and affected by several factors, and trying to explain this quickly becomes speculations. Still, it is interesting to consider how electrons are distributed in the states due to the BZ projection. We know that the 1Δ states are associated with 4 of the 6 degeneracy lobes of the CBM, while the Γ states derive from the remaining 2. If we were to assume an equal filling fraction for the Γ and the 1Δ states, the electrons states representing the Γ bands (within the same BZ) would be squashed together in the center of the zone, while the electrons residing in the 1Δ bands would be distributed between the four leaves towards the zone corners. This is assumed to affect the measured intensity of the states. Another factor that surely plays a role is that the 1Δ states are measured far away from normal emission, making scattering effects more significant compared to the Γ state measurements.

If we now focus on the curvature of the 1Δ bands for the different samples, we se a clear trend of the bands becoming increasingly narrow as the layer is made thinner. This could indicate that the effective mass of the bands is dependent on the layer thickness. The reasons for this is not immediately clear to me. From my point of view, such an effect would be surprising, as we know that the δ-layer states can be described by the same effective masses as the bulk bands from which they are derived. If such a dramatic change in electronic structure does not change the effective mass, why should a change in layer thickness promote this? I will admit that this is not at all a trivial question. Electron interactions in quantum-confined systems are complex phenomena, and might be relevant to the situation in ways I can not anticipate[4]. I will not attempt to answer this any further. I will however discuss two factors that might influence this observation. First of all, the error in the fits must be taken into account. The curvature of the fitted band parabolae is mainly determined by the MDC fits close to the Fermi level. The quality of the data and the attenuation due to the Fermi step makes this process subject to some uncertainty. The fact that the trend is so consistent across all the samples still indicate that this might be attributed to some other effects. Second, it could indicate that the measurements correspond to different cuts of the BZ as a result of the changing $k_\perp$-dependence of the states. This can be explained in the same way as previously discussed, related to the different photon energies used for measuring the Γ states. The difference here is that we are not measuring at normal emission, which could cause a more dramatic behavior e.g. through refraction effects of the $k_\perp$ component in the photoemission process. Still, this remains speculations, but

[4] For instance through effective mass renormalization [4, 18].

should be kept in mind for further discussion.

6.5 Valley splitting trends for varying δ-layer thickness

In Figure 6.6, the energy band minima of the δ-layer states are shown as a function of δ-layer thickness. The energies are presented in terms of the valley splitting relative to the 1Γ state for the individual samples. This is done for two main reasons: 1) The impact of varying dopant configurations across different samples is reduced, and 2) any energy offsets due to erroneous Fermi level pinning between the different samples are avoided. The arguments behind this choice have been discussed previously, in relation to the 1Γ state energy variation. Additional data points from previous work presented in Ref. [17] are included to extend the data range and to supplement the discussion. The additional data is obtained from ARPES investigation of two samples with 2 nm and 4 nm thick dopant profiles, which were prepared according to a similar scheme as the one used in the work of this text[5].

6.5.1 General trends

The overall trend of the observed $1\Gamma - 2\Gamma$ valley splitting is similar to the SW model calculations, with the splitting increasing as the layer is made thinner. This is seen as a consequence of the increased confinement, pushing the energy levels apart. For the thickest sample, the two states are degenerate in energy. This is as expected for a bulk-like sample, due to the fact that both states originate from the same bulk state associated with the CBM. If we now look at the $1\Gamma - 1\Delta$ splitting, there are two main observations I wish to address. The most striking aspect is the almost parabolic feature that crosses the $1\Gamma - 2\Gamma$ trend. The energy increase for the thicker layers is especially interesting, as we would expect all three states to be degenerate in the bulk-like case. One explanation could be that the thickest layer is not sufficient to produce a true bulk-like behavior. In this view, it is possible that the 1Δ has split apart from the Γ states in the 4 nm sample, but the confinement is not yet strong enough to break the Γ state degeneracy. The downward trend of the 1Δ as the layer is made thinner could then be explained by a charge redistribution effect due to electron migration that occurs as the Γ

[5]It should be mentioned that these samples lack a capping layer, which may cause the states to be found at slightly different binding energies due to the implications of the potential. Without a capping layer, the potential step of the δ-layer will be altered by the vacuum boundary at the surface. Dopant diffusion is also limited to one perpendicular direction. These deviations are estimated to be negligible for the purposes of this discussion.

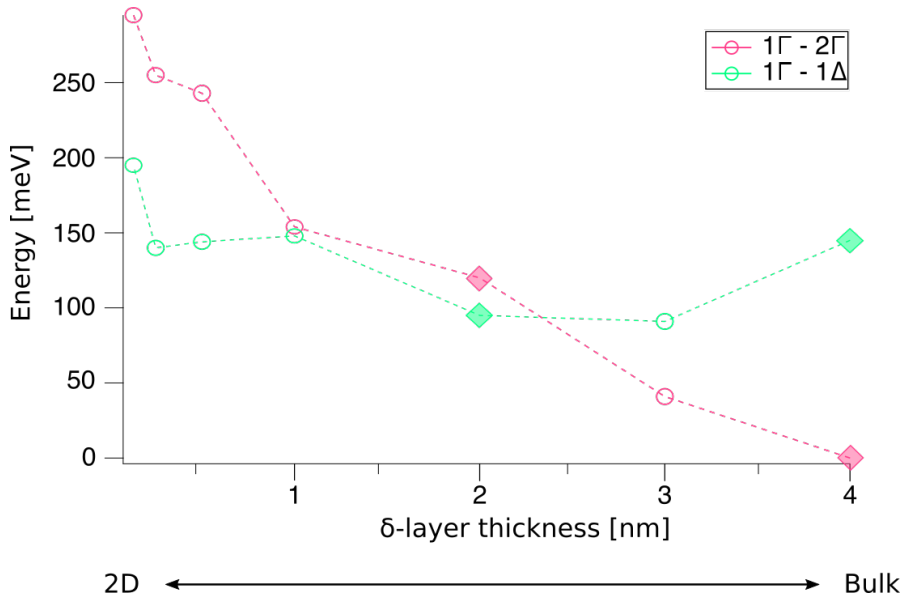

Figure 6.6: δ-layer state energy separation versus layer thickness. Measured band minima energies of the 2Γ (magenta) and 1Δ (green) states are plotted relative to the 1Γ state energy (valley splitting). Data points for 4 nm and 2 nm layers are included from the previous work presented in Ref. [17], indicated by filled diamonds.

states split apart, bringing down the 1Δ state in energy as the 2Γ is raised. An alternative view can be taken by comparing to the SW model results. Apart from the energy scale, there is a clear resemblance between the observed trend and the predictions presented in Figure 5.3. Previous discussion regarding the model justifies a possible energy shift of the 1Δ state compared to the 1Γ state (Sec. 5.1). This could indicate that the trend is caused by the different effective masses of the bands, and that the raising of the 1Δ for thicker layers is a real effect of the confinement. However, the best match is achieved for the calculations using weak potentials, which are not expected to be able to produce the degree of confinement we see in the Γ states measurements. This could be an effect of lacking accuracy of the model. There is also the chance that we are not actually probing the CMB for the thicker layers. This can be seen in relation to the previously discussed variations in curvature of the 1Δ state bands, which could indicate that some translation in momentum space takes place. This could cause an energy shift due to the increased $k_\perp$-dependancy of the thicker layer states. Again, this quickly becomes speculations. It is safe to say that the observed trend is hard to explain by any one effect. Many competing factors contribute to the dynamics of the electron states as the layer is made increasingly bulk-like, and it is likely that some superposition of 2D and 3D state characteristics is present in the thick layer

measurements.

A more subtle trend for the 1Δ splitting can be seen for the thinnest samples, where the state seems to make a small "dip" compared to the 1Γ state. This happens right around the point where the 2Γ disappears above the Fermi level, indicating that this too could be related to some charge redistribution. It should be noted that the uncertainty of the fits might influence the magnitude of the observed trend.

6.5.2 Monolayer valley spliting

In Section 2.4 we saw that previous work has not been able to completely reconcile experimental observations and theoretical predictions for the monolayer case. It is therefore natural to focus on the monolayer measurements to see how the data relates to the established picture. In particular, I will discuss the ordering of the states, and how a change in the dielectric constant could help explain the observed behavior.

By comparing to previous tight-binding calculations, we see that the measured $1\Gamma - 2\Gamma$ valley splitting is roughly 10 times larger than the predicted value. This is a significant deviation, and could indicate a lack of understanding of the situation. We should immediately address the fact that the calculations assume a lower dopant density (25%) than we can expect for the investigated sample ($\leq 50\%$[6]). However, the calculations predict that this change in dopant density should not affect the $1\Gamma - 2\Gamma$ band splitting to any significant degree, at least not of the magnitude that is observed. This contradiction is reinforced by comparing to existing experimental monolayer data. The presented measurements of the double-dosed monolayer show a dramatic increase ($\approx \times 2$) in the $1\Gamma - 2\Gamma$ valley splitting compared to single-dosed monolayer data presented in Ref. [28] (see Figure 2.11), indicating a large dependence on the dopant density. Figure 6.6 also show that the 1Δ state minima sits in between the 1Γ and 2Γ state in the measurements, contradicting the predicted ordering that puts the 1Δ as the highest energy state of the three. These observations could serve to support that the state referred to as 2Γ in the measurements is in fact the 3Γ state, as suggested in Ref. [25]. This would mean that the observed 1Γ band actually contains a second band, even though there is no compelling evidence for this in the data. This could still be possible, as the predicted magnitude of this splitting is right at the edge of what is possible to resolve through this ARPES experiment. Further investigation on this matter would be needed to clarify this situation.

A problem that arises with this "new" interpretation is that when assuming

[6] Even though the dopant density might be as high as 50%, we might expect the effective number of active carriers to be less due to some dopant deactivation effects (see Section 4.4.)

a bulk Si dielectric constant for the δ-layer, the 3Γ band valley is predicted to be surrounded by other band features which do not appear in the measurements (see Figure 2.10a)[7]. An increase in dielectric constant as suggested by Ref. [25] will disentangle the higher states and produce a distinct, parabolic band valley for the 3Γ (as seen in Figure 2.12), increasing the agreement with the measurements. Still, the observed splittings does not completely match the predictions. This might be affected by several factors. In addition to shifting the Fermi level, the increased dopant density in the measured sample may contribute to altering the band splittings. Even though the $1\Gamma - 2\Gamma$ valley splitting is not expected to vary much with a change in dopant density, the effect may be stronger for the $1\Gamma - 3\Gamma$ and $1\Gamma - 1\Delta$ splittings. We have also seen that tight-binding approaches are known to underestimate the magnitude of the splittings. If these effects are to account for the observed splittings, an important question arises. A general increase in valley splittings in the calculations would indicate that the $1\Gamma - 2\Gamma$ splitting should increase as well, meaning that we should be able to resolve them in the measurements. Why, then, is this not the case in the observations? A possible explanation could be related to the fact that the 1Γ and 2Γ states differ in character from the 3Γ state by being derived from the exact same bulk state, resulting from the broken degeneracy of the two projected out-of-plane lobes of the CBM[8]. This may cause a different behavior of the state splittings compared to other bands such as the 3Γ. Indications of such an effect is also present in the calculations of Ref. [25], which show a near-independent relationship between the $1\Gamma - 2\Gamma$ splitting and the change in dielectric constant, while the higher Γ state bands are affected in a much more dramatic way. If this is the case, this could mean that the relative splittings of the monolayer are artificially high in the overall picture of Figure 6.6 due to the effect the increased dopant density of the layer might have on the state separations.

Finally, we must remember that the data point corresponding to the 2Γ state minima is related to large uncertainty due to the assumptions made. However, it is not likely that the state is located at a significantly lower energy than stated. Instead, it might well be located at a higher energy. With these factors taken into account, it is indeed possible that an increase in dielectric constant could be justifiable to explain the presented monolayer data. Nevertheless, I will not draw any firm conclusions on this matter based on the presented discussion, considering all the complicated effects that are at play in determining the properties of this system.

[7] In Ref. [22], the predicted band structure for a larger dopant density comparable to the investigated monolayer sample is presented. This shows a similar trend for the 3Γ state.

[8] More details on this matter can be found e.g. in Ref. [38].

Chapter 7

Conclusion

This thesis has described the fabrication and investigation of thin, heavily phosphorus-doped profiles in silicon, so-called Si:P δ-layers. The formation of such a layer creates a quantum well perpendicular to the layer, giving rise to confined, highly localized electronic states. The aim of the investigation has been to observe the electronic band dispersion of the three lowest energy states of the layer, called 1Γ, 2Γ and 1Δ, as the dopant layer thickness is varied. In particular, the energy separation of the band minima, called the valley splitting, has been of interest. This supplements existing research on such devices, which mainly concerns the atomically sharp monolayer profiles. The understanding of the energy configuration of these systems is of great interest for the development of silicon-based quantum computing architectures. The experimental work was carried out at the ASTRID2 synchrotron facility in Aarhus, Denmark. Five different samples were prepared, with dopant layer thickness ranging from 3 nm to a true monolayer (≈ 0.13 nm) which were buried under a 1.5 nm thick capping layer of Si. The samples were characterized using angle-resolved photoemission spectroscopy (ARPES). The imaging of the buried states is made possible through resonant enhancement, which constitute a key part of understanding the photoemission process of these structures. As simple numerical model based on a finite square potential well was employed to gain a theoretical framework for discussing the observations.

7.1 Summary of main findings

- The 1Γ state was used as an energy reference for the valley separations. In relation to this, the energy variations of the 1Γ state across the samples was discussed, relating it to changes in dopant density due to the preparation process and charge redistribution effects resulting from the changing band structure. The results showed indications of sensitivity to variations in the

preparation process, mainly due to the delicate temperature dependence of the processes affecting the dopant configuration in the δ-layer.

- Experimental evidence of the 1Δ state for a true monolayer was presented for the first time, allowing comparison to existing work. The occupancy of the band was seen as a consequence of a double-dose preparation scheme, producing enhanced dopant density in the layer compared to normal saturation.

- The overall trend of the Γ state splittings were found to be in good agreement with the predictions from the presented numerical square well model. The 1Δ state was seen to deviate from the expected behavior for thicker layers, showing a near-parabolic trend that crossed the Γ trend line. Comparison to the numerical model indicated that the observed behavior could be related to a difference in effective mass of the Γ and 1Δ bands. An increase towards bulk-like behavior of the states and the accuracy of the model was also seen as a contributing factors. This situation remains inconclusive.

- The band configuration in the particular case of the monolayer was treated in detail. The $1\Gamma - 2\Gamma$ valley splitting was observed to be dramatically larger than previous calculations and measurements, suggesting a review of the state identification. In particular, the observations indicated that the state previously referred to as 2Γ should instead be associated with the predicted 3Γ state. The novel 1Δ monolayer data was found to support this claim, providing new and important insight into the dynamics of this system. The new view suggest that an increase in the previously assumed value for the material dielectric constant is required to reconcile observations and theoretical predictions. This may have significant implications on the electronic properties of the system, an understanding of which might prove important for accurate device prediction and development in the future.

7.2 Looking ahead

The discussion has highlighted some features of the presented results that require further investigation. The most pressing matter is attempting to resolve any near-degenerate states in the lowest Γ band, which is important to clarify the current situation of the monolayer band structure. A success in doing so would represent a compelling argument in support of the suggestions made in this thesis regarding the state identification. Specifically, low-temperature ARPES measurements of super-saturated monolayers could be successful in resolving the states through increasing the band separation while reducing the thermal broadening of the states.

Another point that poses interesting questions is the observed trend of the 1Δ splitting. Investigation of thicker layers to extend the trends towards an increasingly bulk-like situation could provide some answers to this behavior. In this case, the implications of changing the photon energy could be explored to gain a better understanding of how the state configuration behaves as the states become dominated by three-dimensional characteristics.

ARPES only gives information about the occupied electronic states of the material, which limits the investigation of the δ-layer states to below the Fermi level. This is unfortunate, as there are clearly a lot of interesting things happening around and above this region. Inverse photoemission spectroscopy (IPES) is a complimentary technique to regular photoemission, allowing for the probing of unoccupied electron states above the Fermi level [33]. Applying this technique to the study of δ-layers would be a natural continuation of this work, which could contribute vital information on the behavior of the electronic states.

From what has been observed, it is evident that the dopant configuration of the layer plays a major role in affecting the energy of the states. To better understand the measured band structures it would be beneficial to have some idea of the doping properties of the investigated samples. This could be achieved by complementing the photoemission data with electrical measurements of the layers, for instance through depth-dependent four-point-probe- or work function measurements [1, 26].

Appendices

Appendix A

Additional sample preparation data

A.1 Silicon deposition rate

This appendix describes how the silicon deposition rate used for estimating the δ-layer- and capping layer thickness was found. I will start with a quick introduction of the x-ray photoemission spectroscopy technique (XPS), which this approach was based upon.

A.1.1 XPS

X-ray photoemission spectroscopy is a technique mainly used for chemical analysis of a sample. The technique utilizes X-rays to probe the binding energy of core level electrons, by the same principles as illustrated in Figure 3.1. The principle of electron detection is the same as in ARPES, only without the angular dimension (see section 3.1.2). A XPS spectrum can give in-depth information on the chemical environment of the sample as well as the chemical states of the various surface elements [16].

A.1.2 Calibration of the Si deposition rate

The silicon deposition rate was determined by stepwise growing silicon on a Si:P δ-layer and measuring the intensity of the P 2p core levels by XPS in between each growth step. The integrated electron counts belonging to the core level peak served as a measure of the peak intensity. When measuring at normal emission, the initial intensity I_0 of a buried P core level can be related to the measured

intensity I with an overgrown silicon layer of thickness d by the equation

$$I = I_0 e^{-\frac{d}{\lambda}}, \tag{A.1}$$

where λ is the electron inelastic mean free path. In this work $\lambda = 0.7 \pm 0.1$ nm was assumed (in accordance with the universal curve of mean free path (MFP) [17]). The measured intensity and the corresponding calculated deposition rates can be seen in Table A.1.

t [min]	Total counts [10^3 electrons]	d [nm]	Deposition rate [nm/min]
0	24.5	0	-
10	15.3	0.328	0.033
20	8.1	0.772	0.039

Table A.1: Silicon deposition rate.

It has previously been shown that that the growth rate stabilizes for longer deposition times [17]. In the work of this thesis, a Si deposition rate of 0.4 Å/min has been used. Using an uncertainty of 10% in the MFP and the square root of the intensity, the total uncertainty is estimated to be 0.0043 nm/min. The implications of this on the uncertainties for the δ-layer growth parameters is given i Table A.2.

Table A.2: Sample parameters. t_δ and t_{cap} is the δ-layer and capping layer deposition time, respectively. d_δ and d_{cap} is the estimated δ-layer and capping layer thickness, respectively.

Sample ID	t_δ [min]	d_δ [nm]	t_{cap} [min]	d_{cap} [nm]
Beamtime 1				
A	75	3.0 ± 0.3	37.5	1.5 ± 0.2
B	25	1.0 ± 0.1	37.5	1.5 ± 0.2
Beamtime 1				
C	13	0.5 ± 0.05	37.5	1.5 ± 0.2
D	6.5	0.25 ± 0.03	37.5	1.5 ± 0.2
E	double PH_3 dose (monolayer)	≈ 0.13	37.5	1.5 ± 0.2

A.2 Voltage supply parameters

Temperature control was done by limiting current on voltage supplies during direct heating of evaporator and samples. The parameters used are shown in Table A.3.

In addition, the temperature was monitored by an IR pyrometer.

Table A.3: Voltage supply parameters.

Object	Event	Current
Si evaporator	Si evaporation	12.0 A
Sample	Degassing (550°C)	0.85 A
Sample	Flash (1100°C)	11.0 A
Sample	Flash (1200°C)	11.5 A
Sample	Anneal (570°C)	1.1 A
Sample	Anneal (500°C)	1.0 A
Sample	Anneal (400°C)	0.8 A

Appendix B

Data fitting

Data fitting and analysis was done using Wavemetrics Igor Pro 7 software.

B.1 Fermi level pinning

The Fermi level was determined by binning data from several energy distribution curves (EDCs) in an angular range selected outside any band features. The background is relatively constant in such a region, and the Fermi step can be observed by a characteristic dip in the signal. A Fermi-Dirac function at room temperature was fitted against this step, estimating the position of the Fermi level. An example is shown in Figure B.1.

Ulstrup et. al. [35] argue that an EDC based approach for Fermi level determination is unstable in practice, and suggest another method using MDC data to track the integrated intensity of a single energy band arm close to the Fermi level. This method becomes difficult for the case of the states we are dealing with, as there are several bands dispersing across the Fermi level in the same location. This means that the Fermi level pinning could be subject to some uncertainty. Still, this is irrelevant in the discussion of the energy splittings, as these will be independent of the Fermi level location.

B.2 Comments on the quality of fits

In general, the EDC fits give accurate peak locations for the band dispersion when dealing with the bottom of the parabolas, but fails as the bands curve upwards. For the MDC approach, it is the other way around. Thus, these two approaches supplement each other in a nice manner. The EDC data ensures accurate location of the minima of the parabolas, while the MDC contributes to predict the curvature. The EDC method is more complicated and prone to errors, as it has

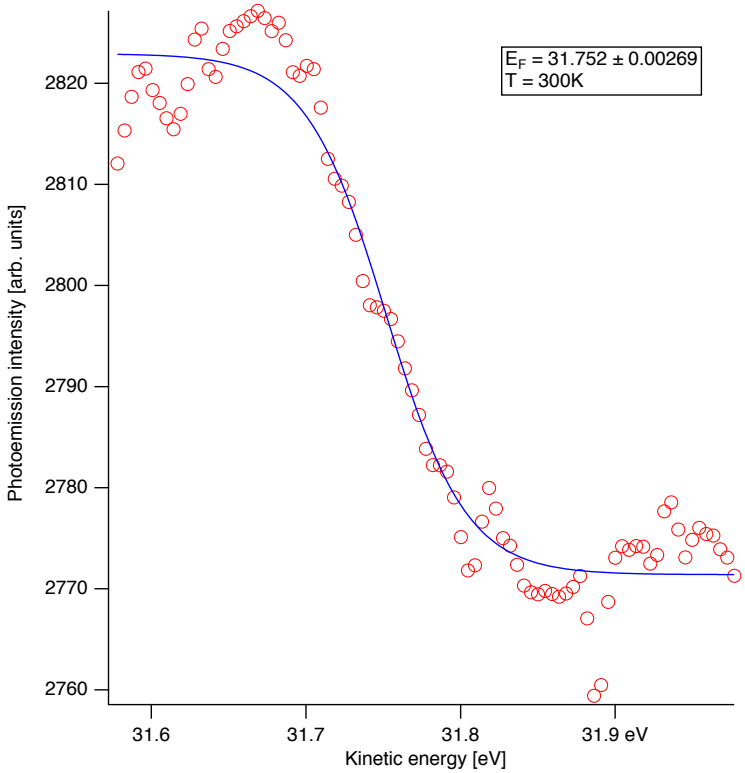

Figure B.1: Fermi level pinning. Sample A with 3 nm dopant profile thickness. Fermi-Dirac distribution at room temperature is fitted to the Fermi step in the intensity of a angle-integrated region containing no band features.

to deal with the bands being affected by the Fermi step. To improve EDC fits a background signal was subtracted, estimated by averaging EDCs within a angular region containing only background noise. This was chosen over a theoretical background subtraction, as this is complex to model in the case at hand [35]. The width of the region was approximately 0.3 Å^{-1} . Considering estimated standard deviations from the fitting process, the error related to the band minima is estimated to be in the order of 10 meV. It should be noted that the fitted bands to the states located above the Fermi level (as is the case for the 2Γ state in the three thinnest samples) is subject to a larger uncertainty, as discussed in the main text.

All of the EDC fitting results show a discrepancy around the Fermi level step. This may indicate that there is a systematic error in the fitting process, such as a offset of the Fermi level or a too narrow Fermi profile in the fitting function. Broadening of the Fermi function may be achieved by modeling assuming increased temperature or by including a energy resolution effect. Better fits are achieved by increasing the temperature by 150 - 200 K. Even though the samples may be subject to some heating from the synchrotron beam, I can not find the physical grounds for such a large temperature increase. A resolution broadening was also modeled by convolving the modulating Fermi function with a Gaussian profile with a full-width half maximum (FWHM) corresponding to the resolution of the instrumentation used. Results are barely affected by this, and such an approach is therefore discarded in favor of the simpler approach in the presented fits.

Appendix C

SGM-3 beamline specifications

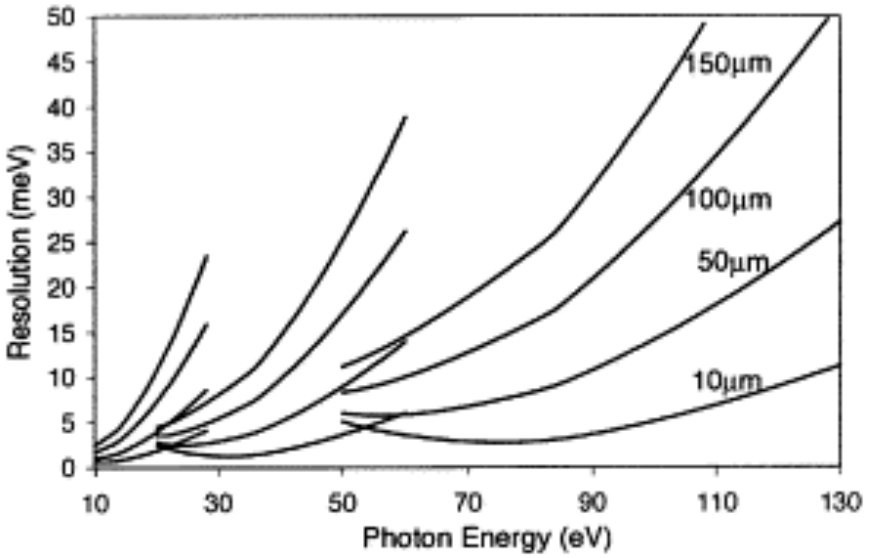

Figure C.1: SGM-3 beamline total resolution for different slit settings. From Ref. [14].

Table C.1: SGM-3 system parameter ranges. Retrieved from Ref. [6].

Parameter	Range / Description
Photon energy $h\nu$	12 - 150 eV
Energy resolution	Better than 10 meV
Angular resolution	Better than 0.1°
Background pressure	$5 \cdot 10^{-11}$ - $2 \cdot 10^{-8}$ mbar
Sample temperature	25 - 1300 K
25 - 400 K manipulator	6 axis
70 - 600 K manipulator	5 axis
180 - 1300 K manipulator	4 axis

Bibliography

[1]F. G. Allen and G. W. Gobeli, "Work function, photoelectric threshold, and surface states of atomically clean silicon", Physical Review **127**, 150–158 (1962).

[2]G. M. Alonzo-Medina, A. González-González, J. L. Sacedón, and A. I. Oliva, "Understanding the thermal annealing process on metallic thin films", in Iop conference series: materials science and engineering (2013).

[3]N. D. Ashcroft, Neil W. ; Mermin, *Solid state physics* (Holt, Rinehart and Winston, New York, 1976).

[4]A. Babinski, M. Korkusinski, P. Hawrylak, M. Potemski, and Z. R. Wasilewski, "Renormalization of effective mass in self-assembled quantum dots due to electron-electron interactions", in Journal of physics: conference series (2013).

[5]M. Benfatto and C. Meneghini, *Synchrotron Radiation* (2015).

[6]P. Bianchi, Marco; Andersen, John E. V.; Kjeldsen, Henrik; Jones, Nykola C.; Hoffmann, Søren V.; Hofmann, *A new multipurpose end-station on the SGM3 beamline @ ASTRID2*, 2014.

[7]B. H. Bransden and C. J. Joachain, *Quantum Mechanics* (Prentice Hall, 2000).

[8]D. J. Carter, O. Warschkow, N. A. Marks, and D. R. McKenzie, "Electronic structure models of phosphorus δ-doped silicon", Phys. Rev. B **79**, 33204 (2009).

[9]A Damascelli, "Probing the electronic structure of complex systems by ARPES", Phys. Scr. (2004) `10.1238/Physica.Topical.109a00061`.

[10]D. W. Drumm, L. C. L. Hollenberg, M. Y. Simmons, and M. Friesen, "Effective mass theory of monolayer δ doping in the high-density limit", **155419**, 1–14 (2012).

[11]D. W. Drumm, A. Budi, M. C. Per, S. P. Russo, and L. C. Hollenberg, "Ab initio calculation of valley splitting in monolayer δ-doped phosphorus in silicon", Nanoscale Research Letters **8**, 1–11 (2013).

[12]M. Fuechsle, J. A. Miwa, S. Mahapatra, H. Ryu, S. Lee, O. Warschkow, L. C. L. Hollenberg, G. Klimeck, and M. Y. Simmons, "A single-atom transistor", Nat Nano **7**, 242–246 (2012).

[13]T. Hallam, "The use and removal of a hydrogen resist on the Si (001) surface for P-in-Si device fabrication", (2006).

[14]P. Hoffmann, Søren V.; Hofmann, *The SGM 3 Beamline at ASTRID*, 2009.

[15]P Hofmann, *Solid State Physics: An Introduction*, Physics textbook (Wiley, 2011).

[16]P Hofmann, *Surface Physics: An Introduction* (Philip Hofmann, 2013).

[17]A. J. U. Holt, "Engineering Quantum States in δ-doped Semiconductors", Masters Thesis (NTNU, 2017).

[18]M. Holzmann, B. Bernu, V. Olevano, R. M. Martin, and D. M. Ceperley, "Renormalization factor and effective mass of the two-dimensional electron gas", Physical Review B - Condensed Matter and Materials Physics (2009) 10.1103/PhysRevB.79.041308.

[19]B. E. Kane, "A silicon-based nuclear spin quantum computer", 133–137 (1998).

[20]J. G. Keizer, S. Koelling, P. M. Koenraad, and M. Y. Simmons, "Suppressing Segregation in Highly Phosphorus Doped Silicon Monolayers", ACS Nano **9** (2015) 10.1021/acsnano.5b06299.

[21]J. G. Keizer, S. R. Mckibbin, and M. Y. Simmons, "The Impact of Dopant Segregation on the Maximum Carrier Density in Si : P Multilayers", 7080–7084 (2015).

[22]S. Lee, H. Ryu, H. Campbell, L. C. L. Hollenberg, M. Y. Simmons, and G. Klimeck, "Electronic structure of realistically extended atomistically resolved disordered Si:P δ-doped layers", Phys. Rev. B **84**, 205309 (2011).

[23]F. Mazzola, "Photoemission spectroscopies and their application in solid state and material physics", PHD thesis (NTNU, 2016).

[24]F. Mazzola, M. T. Edmonds, K. Høydalsvik, D. J. Carter, N. A. Marks, B. C. C. Cowie, L. Thomsen, J. Miwa, M. Y. Simmons, and J. W. Wells, "Determining the Electronic Confinement of a Subsurface Metallic State", ACS Nano **8**, 10223–10228 (2014).

[25]F. Mazzola, C.-y. Chen, R. Rahman, X.-g. Zhu, C. M. Polley, M. Y. Simmons, P. Hofmann, J. A. Miwa, and J. W. Wells, "The Sub-band Structure of Atomically Sharp Dopant Profiles in Silicon", "in preparation", 1–9 (2018).

[26]S. R. McKibbin, C. M. Polley, G Scappucci, J. G. Keizer, and M. Y. Simmons, "Low resistivity, super-saturation phosphorus-in-silicon monolayer doping", Applied Physics Letters **104**, 123502 (2014).

[27]J. A. Miwa, P. Hofmann, M. Y. Simmons, and J. W. Wells, "Direct measurement of the band structure of a buried two-dimensional electron gas", Physical Review Letters **110** (2013) 10.1103/PhysRevLett.110.136801.

[28]J. A. Miwa, O. Warschkow, D. J. Carter, N. A. Marks, F. Mazzola, M. Y. Simmons, and J. W. Wells, "Valley Splitting in a Silicon Quantum Device Platform", Nano Letters **14**, 1515–1519 (2014).

[29]A. Morello, C. C. Escott, H. Huebl, L. H. Willems Van Beveren, L. C. L. Hollenberg, D. N. Jamieson, A. S. Dzurak, and R. G. Clark, "Architecture for high-sensitivity single-shot readout and control of the electron spin of individual donors in silicon", Physical Review B - Condensed Matter and Materials Physics (2009) 10.1103/PhysRevB.80.081307.

[30]J. J. Pla, K. Y. Tan, J. P. Dehollain, W. H. Lim, J. J. L. Morton, D. N. Jamieson, A. S. Dzurak, and A. Morello, "A single-atom electron spin qubit in silicon", Nature **489**, 541–545 (2012).

[31]A Shik, *Quantum Wells: Physics and Electronics of Two-Dimensional Systems* (1998).

[32]J Singh, *Smart Electronic Materials: Fundamentals and Applications* (Cambridge University Press, 2005).

[33]N. V. Smith, "Inverse photoemission", Reports on Progress in Physics, 1227–1294 (1988).

[34]G. C. Tettamanzi, S. J. Hile, M. G. House, M. Fuechsle, S. Rogge, and M. Y. Simmons, "Probing the Quantum States of a Single Atom Transistor at Microwave Frequencies", ACS Nano **11**, 2444–2451 (2017).

[35]S. Ulstrup, J. C. Johannsen, M. Grioni, and P. Hofmann, "Extracting the temperature of hot carriers in time- and angle-resolved photoemission", Review of Scientific Instruments **85**, 1–17 (2014).

[36]O. Warschkow, N. J. Curson, S. R. Schofield, N. A. Marks, H. F. Wilson, M. W. Radny, P. V. Smith, T. C. G. Reusch, D. R. McKenzie, and M. Y. Simmons, "Reaction paths of phosphine dissociation on silicon (001)", The Journal of Chemical Physics **144**, 014705 (2016).

[37]H. F. Wilson, O. Warschkow, N. A. Marks, N. J. Curson, S. R. Schofield, T. C. G. Reusch, M. W. Radny, P. V. Smith, D. R. McKenzie, and M. Y. Simmons, "Thermal dissociation and desorption of PH3 on Si(001): A reinterpretation of spectroscopic data", Physical Review B (2006) 10.1103/PhysRevB.74.195310.

[38]F. A. Zwanenburg, A. S. Dzurak, A. Morello, M. Y. Simmons, L. C. L. Hollenberg, G. Klimeck, S. Rogge, S. N. Coppersmith, and M. A. Eriksson, "Silicon quantum electronics", Rev. Mod. Phys. **85**, 961–1019 (2013).